NASA CR-54213
GE 214-252 (1 SAR)

CYCLOTRON RESONANCE PROPULSION SYSTEM

by

David B. Miller and George W. Bethke

prepared for

NATIONAL AERONAUTICS AND SPACE ADMINISTRATION

contract NAS 3-6266

SPACE SCIENCES LABORATORY
GENERAL ELECTRIC
MISSILE AND SPACE DIVISION

Requests for copies of this report should be referred to

National Aeronautics and Space Administration
Office of Scientific and Technical Information
Attention: AFSS-A
Washington, D.C. 20546

GENERAL ELECTRIC
COMPANY

VALLEY FORGE SPACE TECHNOLOGY CENTER (MAIL: P. O. BOX 8555, PHILA., PA. 19101) . . TEL. 969-2000

MISSILE AND
SPACE DIVISION

SPACE SCIENCES
LABORATORY

May 18, 1965

First Semiannual Report
Contract No. NAS 3-6266
GE Requisition No. 214-252

Gentlemen:

The enclosed report for the subject contract is sent to you for perusal and retention in accordance with the distribution list furnished by the National Aeronautics and Space Administration.

K. E. Paschall

K. E. Paschall
Editor
Space Sciences Laboratory

/rmk

enc.

NASA CR-54213
GE 214-252(1 SAR)

SEMIANNUAL REPORT

CYCLOTRON RESONANCE PROPULSION SYSTEM

by

David B. Miller and George W. Bethke

prepared for

NATIONAL AERONAUTICS AND SPACE ADMINISTRATION

May 17, 1965

CONTRACT NAS 3-6266

Technical Management
NASA Lewis Research Center
Cleveland, Ohio
Spacecraft Technology Division
Dr. H. G. Kosmahl

GENERAL ELECTRIC COMPANY
SPACE SCIENCES LABORATORY
MISSILE AND SPACE DIVISION
P.O.Box 8555
Philadelphia, Pennsylvania 19101

TABLE OF CONTENTS

ABSTRACT

27691

Two cyclotron-resonance plasma accelerators have been built. Both are of the longitudinal-interaction type, and each has a 1.152 inch inside diameter. One features axial injection of the propellant through a hole in the waveguide window. Peripheral injection is employed in the other. A total calorimeter, an array of diode probes, an energy analyser, and potential probes have to date been employed to study the exhaust stream. The axial injection accelerator has been shown to have relatively low power efficiency (a maximum of 42% of the r-f power was observed in the exhaust stream) and the window design is not structurally adequate. Preliminary diode probe array studies of the peripheral injection accelerator indicate that the efficiency may be better. The energy analyser probe has shown that the ions have mean energies of 57-197 ev with spreads of ± 15-35%.

Author

1. INTRODUCTION

This report covers the results accomplished during the first six months of a study supported by NASA Contract NA3-6266. This is the most recent phase of a NASA-sponsored program (earlier Contract Nos. NAS5-1046 and NAS3-3567) to develop an r-f driven electron-cyclotron resonance plasma accelerator for space propulsion applications. Previous to this current program, an accelerator having the following characteristics had been developed.

1). Steady state operation (engine temperature having reached a steady equilibrium value) at up to 4150 watts r-f input power.

2). Over 50% transfer of r-f input power to power in the accelerated plasma jet emerging from the engine.

The objectives of these current studies are basically three fold:

1). Improve the engine performance by improving the accelerator design.

2). Improve the engine performance by gaining a more thorough understanding of the important operating processes within the accelerator.

3). Obtain a more complete measure of the engine thrust characteristics.

The first objective is being sought by two new basic accelerator designs and a shortened variation of each. The second and third objectives are being pursued by application of a variety of diagnostics techniques.

As of this writing, only one of the basic designs has received a thorough study. The result of this study is that the design did not improve operating characteristics and in addition had structural weaknesses which became evident during testing. The alternate configuration has not yet been evaluated sufficiently to make any judgment yet of its qualifications. The various diagnostics techniques have for the most part either been brought into use or are well along to the point of application.

This report will first describe the experimental equipment: facilities, accelerators and diagnostics instruments. Results to date will then be gathered together.

2. EXPERIMENTAL EQUIPMENT

2.1 Test Facility

The experimental work for this contract is being carried out in a new Test Facility, financed by General Electric facility funds. This facility, shown in the accompanying photographs and diagram (Figures 1, 2 and 3) has the following specifications:

vacuum tank: 4' diameter, 6' long, full-sized hinged doors each end, stainless steel.

pumping system: (2) oil diffusion pumps, each rated at 18,000 liters per second; estimated total pumping capacity (taking into account flow resistance due to right angle valves and baffles) is 9000 liters per second (20,000 liters per second without the baffles).

ultimate attained pressure: 1.6×10^{-7} mm Hg (without liquid nitrogen in baffles).

high voltage power supply: 12.5 - 16 k v d c, 3 amperes maximum. (three phase full-wave bridge circuit).

2.2 Thrustors

The two basic accelerator designs are shown in Figures 4 and 5. Continuing the accelerator designation system begun for X-band accelerators during Contract NAS3-3567, these will be referred to as the Mark IV and Mark V designs.

The Mark IV-L thrustor (Figure 4; the L designation indicating the long version) is an axial-injection configuration in which the propellant gas is injected from a pressure chamber into the plasma acceleration chamber through a small diameter hole drilled completely through the ceramic dielectric window. The smallest hole which the window vendor was able to

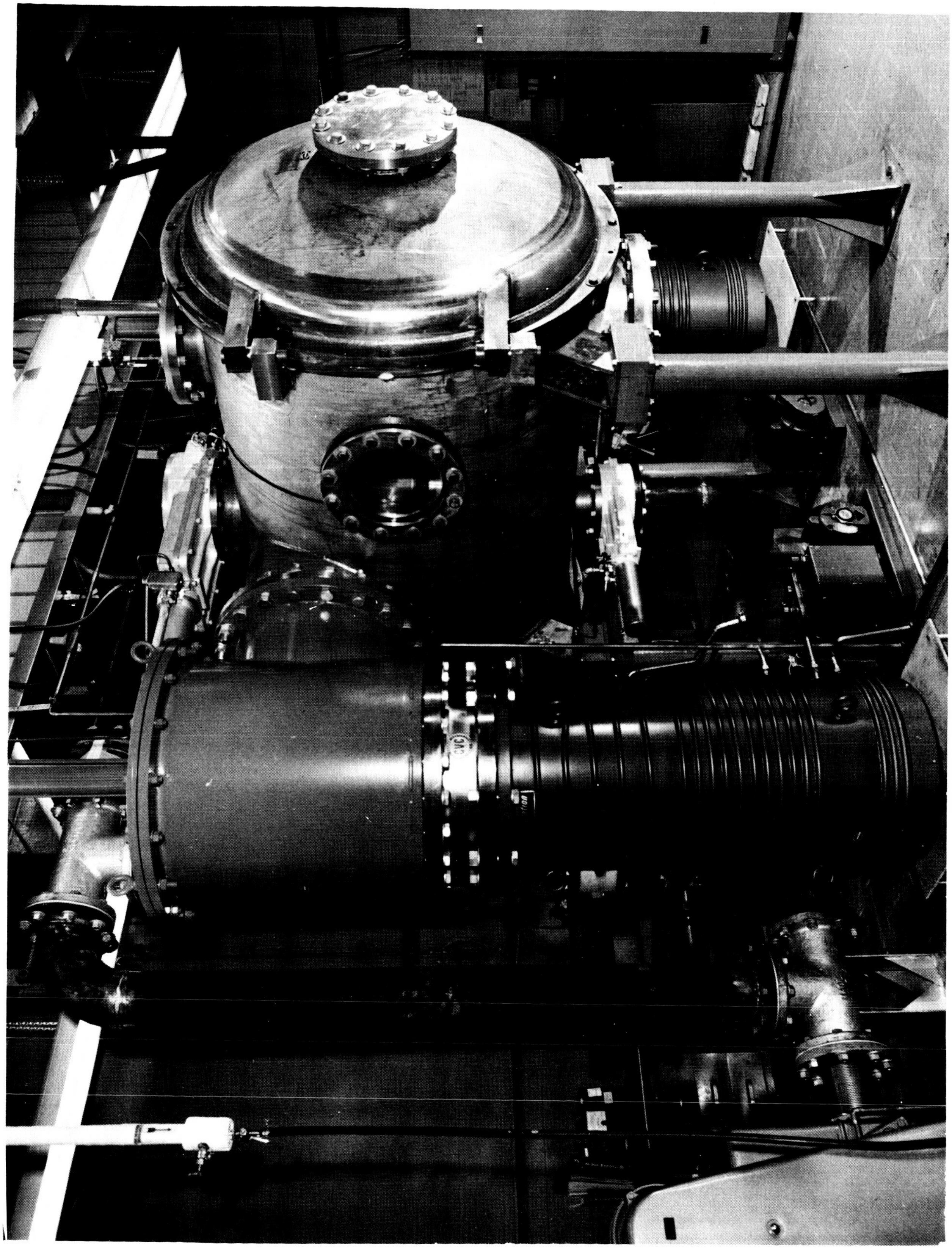

Figure 1. Vacuum Facility

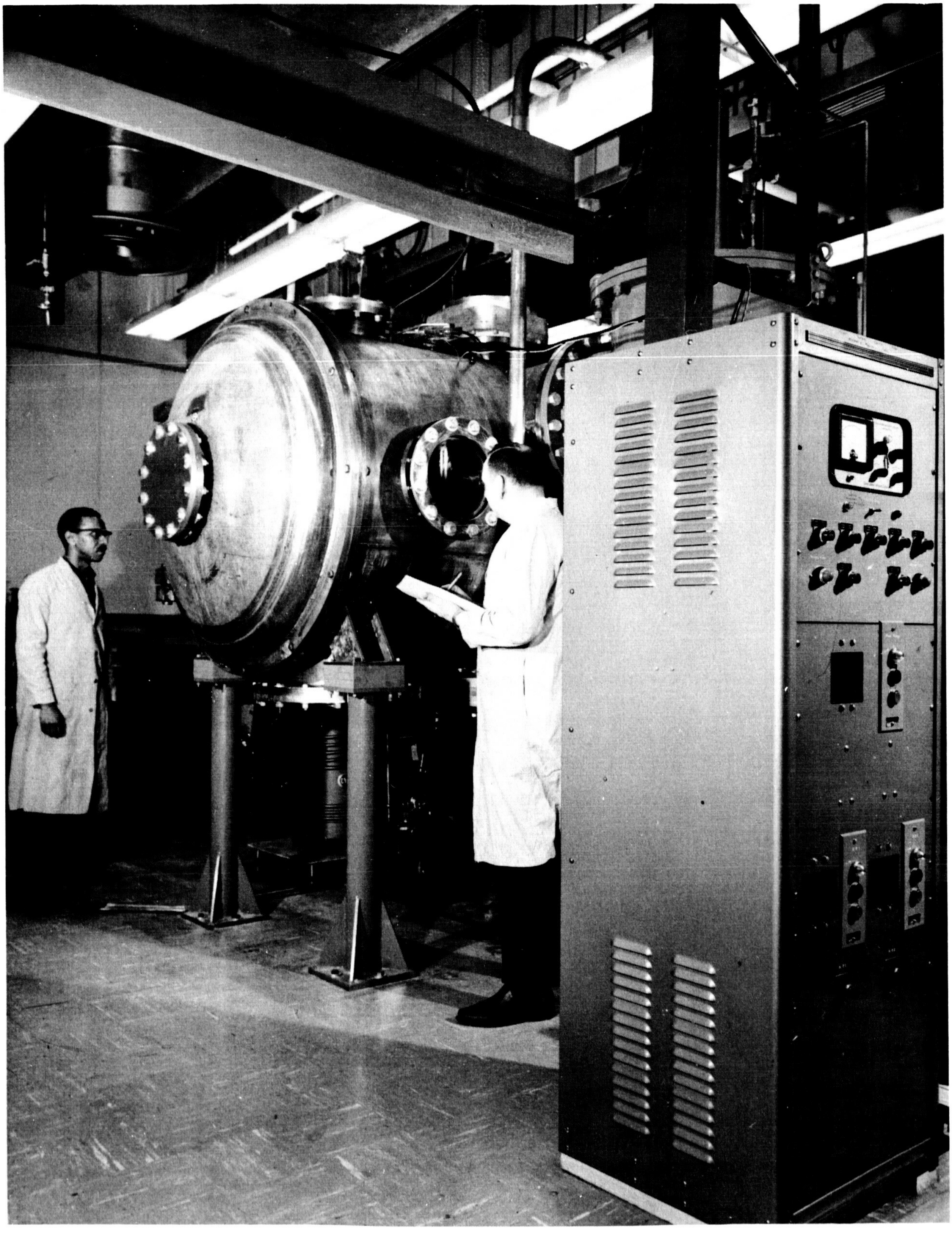

Figure 2. Vacuum Facility

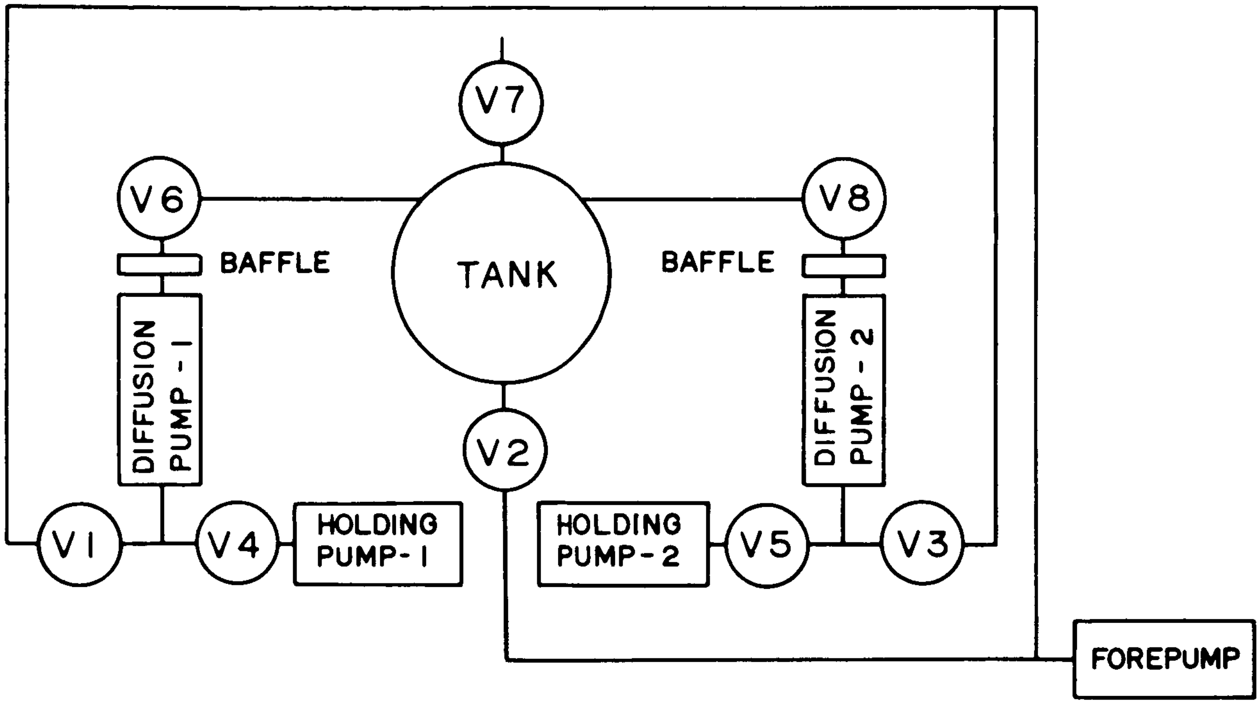

Tank: 4' Dia x 6' Long

Baffles: CVC BC210

Pumps:

Diffusion: CVC PMC 18000
Fore: Stokes 212H
Holding: Welch 1403B

Valves:

V1, V2, V3: 6" Gate, CVC VST 63M2
V4, V5: 2" Gate, CVC VST 23M2
V6, V8: 20" Rt. Angle, CVC VRA 216
V7: 10" Gate, CVC VST 103M2

Figure 3. Vacuum System - Microwave Physics Laboratory

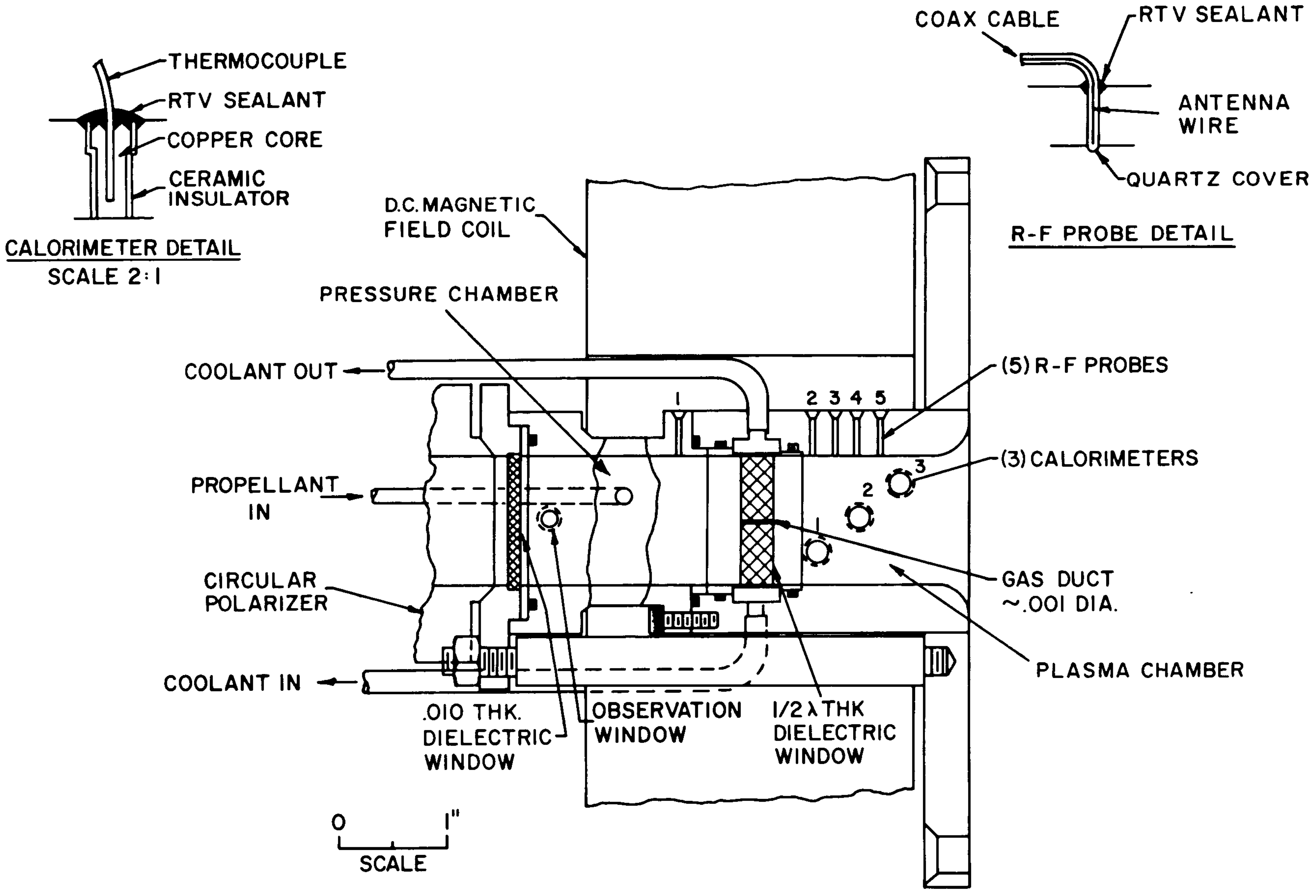

Figure 4. X-Band Longitudinal - Interaction Accelerator; Axial Injection (Mark IV)

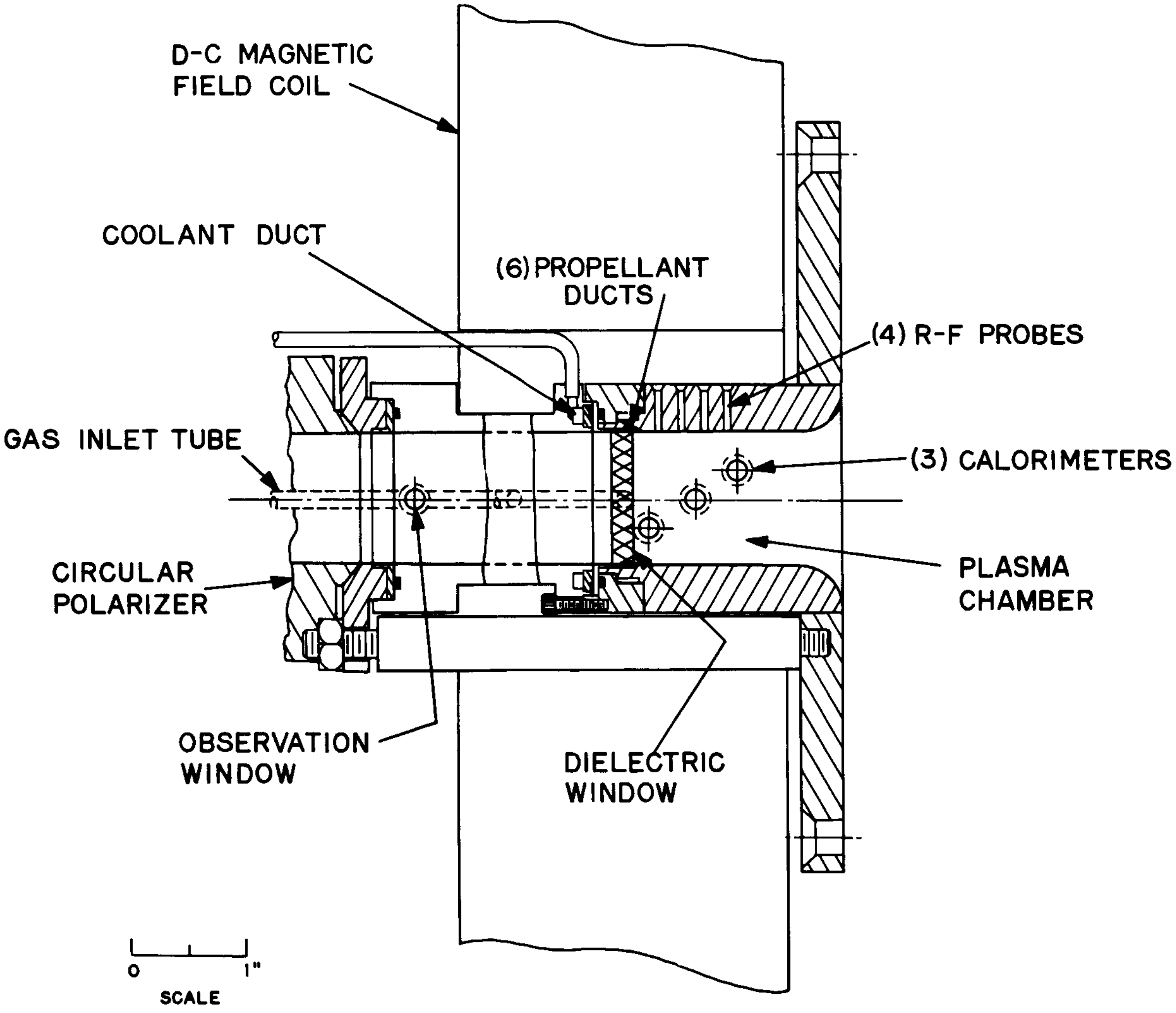

Figure 5. X-Band Longitudinal-Interaction Accelerator; Peripheral Injection (Mark V)

put through these ceramic pieces was approximately .015 inches in diameter. In order to reduce the propellant flow to the desired levels, however, the pressure chamber had to be held down at such a low pressure ($\sim$ 50 torr absolute) that a shielding (and damaging) discharge formed in this inter window region. This undesirable phenomenon was cured by filling the original .015 gas hole with a high-temperature electrically-insulating cement (Sauereisen type DW-30), leaving a small ($<$.001 diameter) through hole. This resulted in interwindow pressures greater than an atmosphere, high enough in general to prevent interwindow discharges although occasional spurious electrical effects still did take place in this region. These latter phenomena might have been related to behavior of the cement, which was observed to exhibit some small amount of reaction to the high-power r-f. Over the course of perhaps 10^3 seconds operation, erosion of the cement, indicated by increased flow for a given pressure, was also observed. Thus, if this technique were to be employed in a final engine, a much more satisfactory filling material must be found.

Both high purity alumina and beryllia were employed for the thick ($1/2\,\lambda$) window in the Mark IV accelerator. Apparently the hole through the window weakened it structually since in all cases the windows eventually developed hairline radial cracks which penetrated through the entire window thickness. The alumina windows failed very rapidly while the beryllia units lasted considerably longer. Note that the window flange was designed with a thin section adjacent to the ceramic and the water cooling. This section was to have been sufficiently flexible to take up any radial strains which might appear in the window, but apparently this measure was inadequate.

The inside diameter of the waveguide through the pressure and plasma chambers is maintained at the 1.152 inch polarizer dimension. Although this results in considerably higher window power density loading than in the two inch diameter Mark I accelerator (see Final Report, NAS3-3567), it is below cutoff for modes above the fundamental TE_{11} mode and so will be less affected by multiple modes and "ghost" modes within the window.

Views of the Mark IV accelerator mounted in operating position on the vacuum tank are shown in Figures 6 and 7.

The short version of the axial injection accelerator (Mark IV-S) is identical with the unit shown in Figure 4 except that the plasma chamber (between the 1/2 λ) window and the right-hand exit plane) has been shortened to one inch. In addition, the wall calorimeters and r-f probes have been eliminated, and the plasma chamber is made of stainless steel rather than copper.

The alternate basic accelerator is shown in Figure 5. In this geometry a single solid dielectric window is used, and the propellant gas is injected peripherally through six angling holes in the plasma chamber wall just on the vacuum side of the window. The same 1.152 inch inside diameter is employed as for the Mark IV design. The short version (Mark V-S) again has a one-inch-long stainless steel plasma chamber without probes and wall calorimeters.

Alumina, beryllia and sapphire windows have been prepared for the Mark V accelerator, the latter (sapphire) being only 0.10 inch thick, while the ceramic windows are one-half wavelength thick. The alumina windows were again noted to crack under any significant plasma loading (e.g., 1 kw). Extensive testing has been performed with two beryllia windows; one failed when the window temperature* was allowed to rise too high, and the second is still functioning satisfactorily.

---

*-A thermocouple is located in the plasma chamber wall adjacent to the window flange.

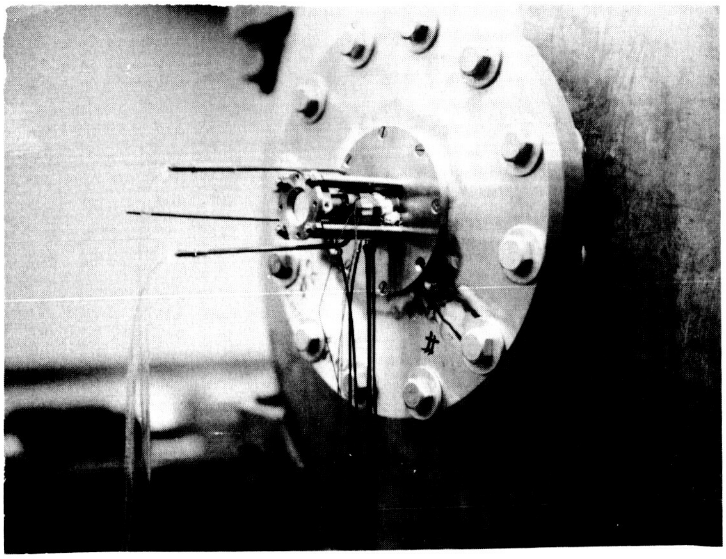

Figure 6. Mark IV (Axial Injection) Accelerator, Mounted on Vacuum Tank.

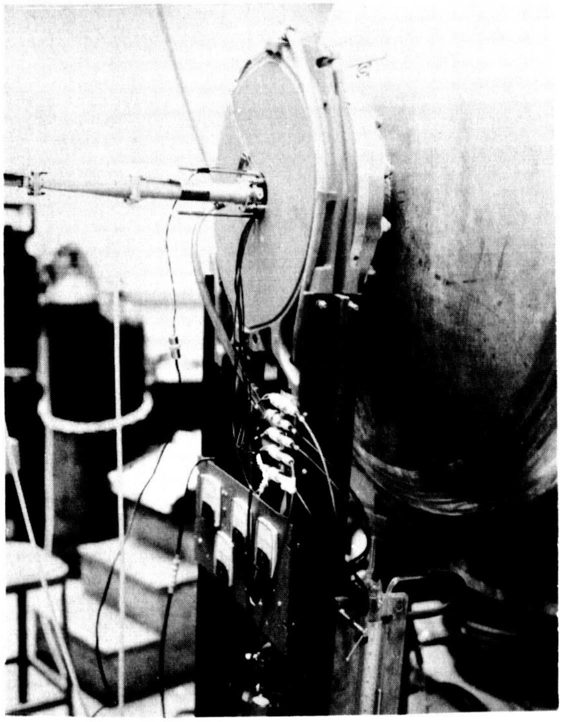

Figure 7. Photograph of Assembled Axial-Injection (Mark IV) Accelerator

2.3 Magnetic Field

A single coil (Magnion "plasma flux" coil, type PF3-285-175) is used with these accelerators, as illustrated in Figures 4 and 5. The resulting on-axis field distribution is plotted in Figure 8. A three-phase bridge rectifier circuit has been built to supply the d-c (up to 292a, 88 v) for this coil.

2.4 R-f System

The r-f system to generate the microwave power is shown in Figure 9. Note that the input r-f power to the accelerator is continuously monitored by a calorimetric power meter. The system, with this power meter, has also been operated into a calibrated water load/calorimeter (Varian, Model V-4045F, Ser. #19), comparing the two absolute power meters up to 5 kw.

2.5 Plasma Diagnostics

2.5.1 Reflection Coefficient

A pair of thermistor power meters in a standard waveguide reflectometer arrangement (see Figure 9) is used to compare incident and reflected power. In addition, these two powers are chart recorded continuously during each run using crystal detectors. In all tests, the tuner is used to minimize the power appearing in the reflected wave traveling back toward the klystron. Because this reflectometer is located several waveguide feet back from the accelerator, power lost in heating the walls of the connecting waveguide are not taken into account either in determining power incident on the plasma or in determining the plasma reflection coefficient. Since losses along such a waveguide are generally small, this correction should also be small.

2.5.2 R-f Probes

R-f probes located in the acceleraor walls (see Figures 4 and 5) respond to the r-f electric field in the vicinity of the probe. The induced signal is rectified through a crystal detector and then recorded on the chart recorder.

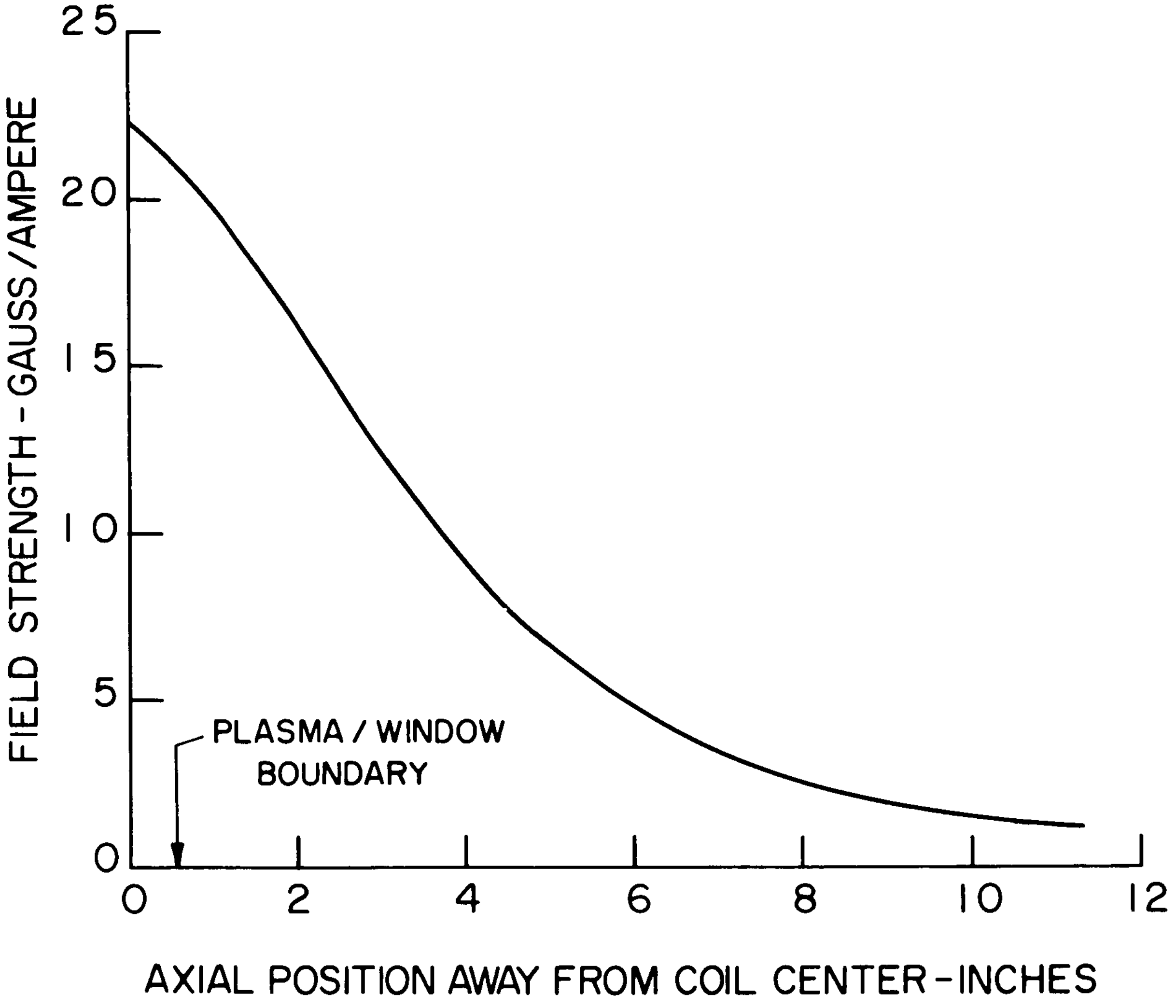

Figure 8. Magnetic Field Distribution on Axis; Magnion "Plasma Flux" Coil, Type PF3-285-175.

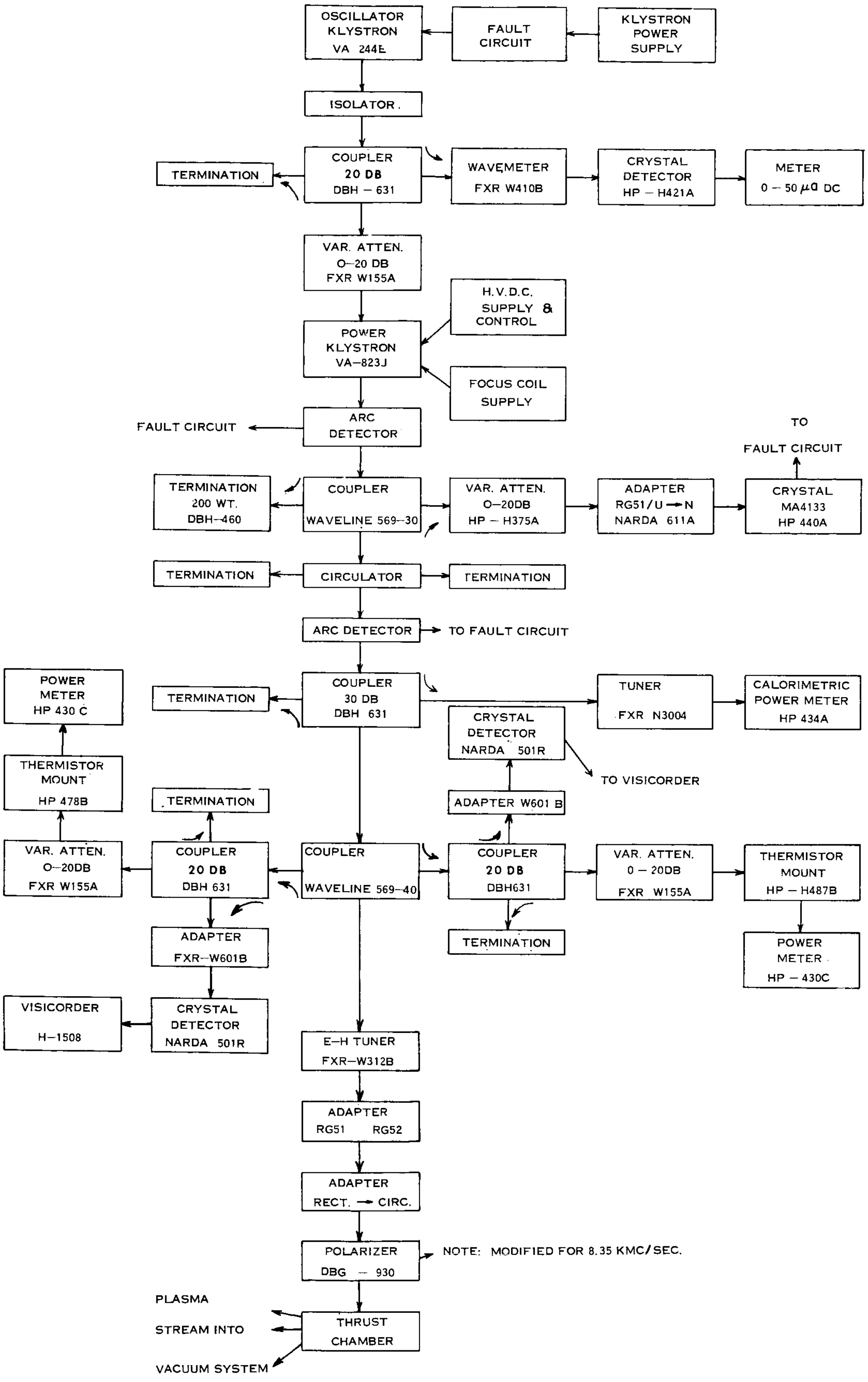

Figure 9. R-f System, Microwave Magnetic Accelerator, 8.35 kmc/sec.

These probes will behave much like the moving probe in a slotted standing wave detector, and the separate probe signals must be interpreted as responding at any instant to the standing wave pattern existing within the accelerator at that instant. It must be remembered, however, that this wave pattern will exist within a lossy medium (plasma) so that the field strength will ultimately go to zero as depth within the plasma increases. Although an attempt was made to make all probes as identical as possible, they will not have identical sensitivities and so will have to be calibrated before they can be used on a comparative basis.

An example of the chart recorder record is shown in Figure 10. The rapid fluctuation causing the wide incident power trace is a 360 cps oscillation probably attributable to the ripple on the 3 phase bridge rectifier circuit d-c supply. The noise on the probe signals is generally present during plasma operation, suggesting that it may be an electromagnetic noise field radiating from the plasma.

2.5.3 Wall Calorimeters

Three button calorimeters are located in the plasma chamber walls of the Mark IV-L and Mark V-L accelerators as shown in Figures 4 and 5. Construction details are shown in Figure 4. These calorimeters are not sufficiently insulated so that they continue to gain temperature throughout a test, but rather they rapidly attain an equilibrium temperature indicative of the power incident on them from the plasma. This power may be calculated from the cooling curve:

$$\Delta T = \Delta T_o \, e^{-t/\tau}$$

where ΔT is the temperature (relative to ultimate) at time t, and ΔT_o is the initial temperature at $t = 0$.

The time constant τ is found to be different for each calorimeter and to be somewhat a function of temperature but is approximately 30 seconds. From

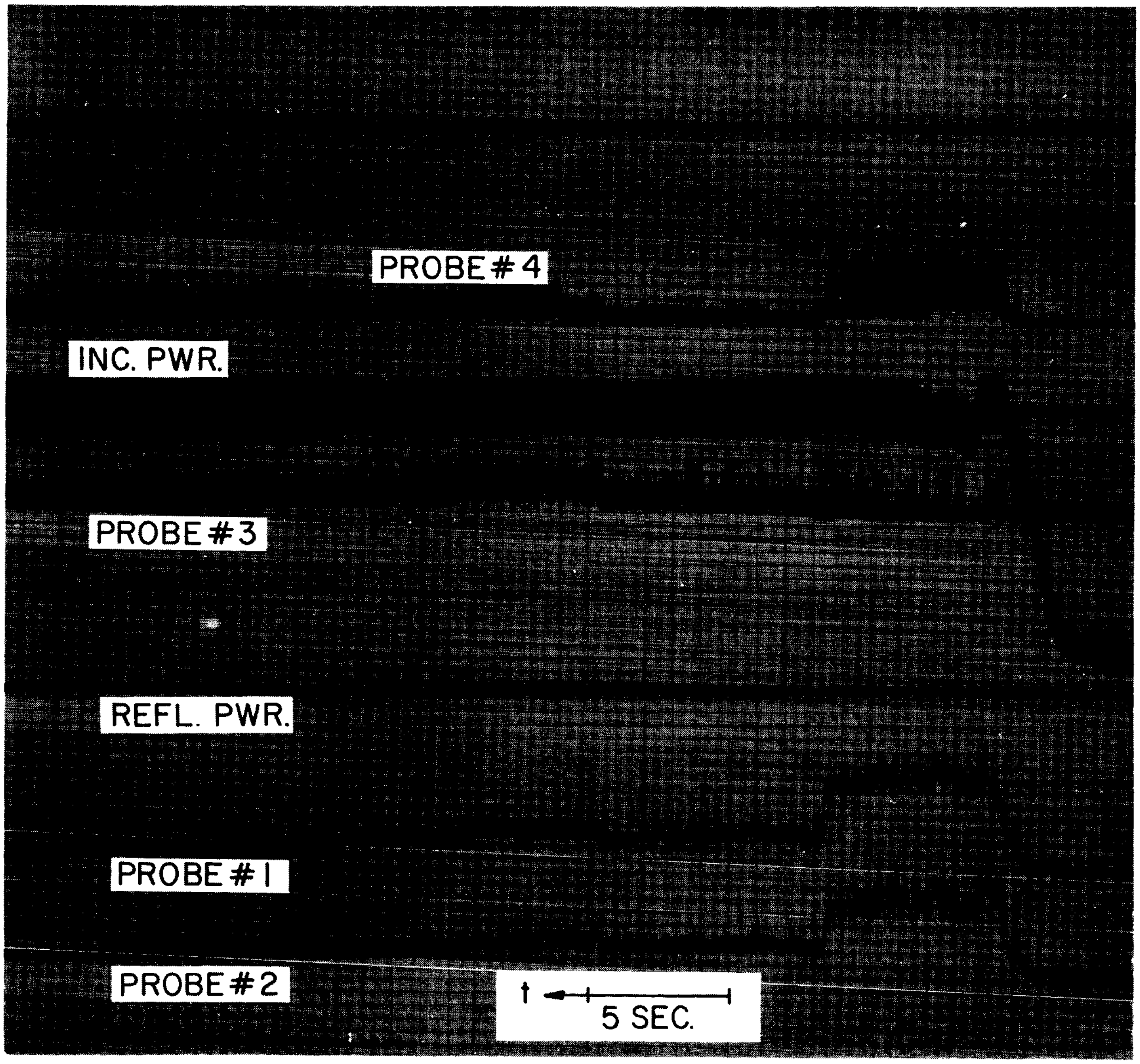

Figure 10. Typical Strip-Chart Recorder Record, Argon, 2 kw, .2 mg/sec, 4060 Gauss at r-f/Plasma Boundary

the cooling expression, the power being lost at any temperature (and therefore the absorbed power) can be derived as:

$$P = -\frac{\sigma M}{\tau} \Delta T$$

where σ is the specific heat ($\sim$ .09 cal/gm - $^{\circ}$C for copper) and M is the mass of the calorimeter. Since the calorimeters have a mass of .77 gm, this amounts to a power loss of about .97 watt from each calorimeter per 100°C calorimeter temperature (Δ T). Converting this to power density by dividing by the known exposed area of the calorimeters (.31 cm^2) and then multiplying by the accelerator wall area (41 cm^2) yields a power of about 1.3 watts going to the accelerator walls per 1° C Δ T.

2.5.4 Total Calorimeter

A large, cylindrical copper calorimeter (2' diameter by 10" deep) has been constructed for plasma stream power measurements. This is water cooled so that steady-state power measurements will be made. It is mounted on a movable shaft so that the plasma power can be measured as a function of distance away from the accelerator. This calorimeter is shown in Figure 11 mounted on its movable platform in the vacuum tank.

The inlet and outlet water temperatures are measured with electrically insulated thermocouples immersed in the water lines at points a few inches before entry into and after emergence from the calorimeter collector. Ice baths are used for the reference junctions. A millivolt recorder (Leeds and Northrup "Speedomax" or Photovolt "Microcord") is used to measure and record the thermocouple e.m.f., as shown in Figure 12. Note that, at a water flow rate of 1500 cc/min, the calorimeter has a time constant of approximately one minute.

2.5.5 Diode Probes

An array of diode probes is being used to map the exhaust stream ion flux density and power density distributions. The probe design is shown in

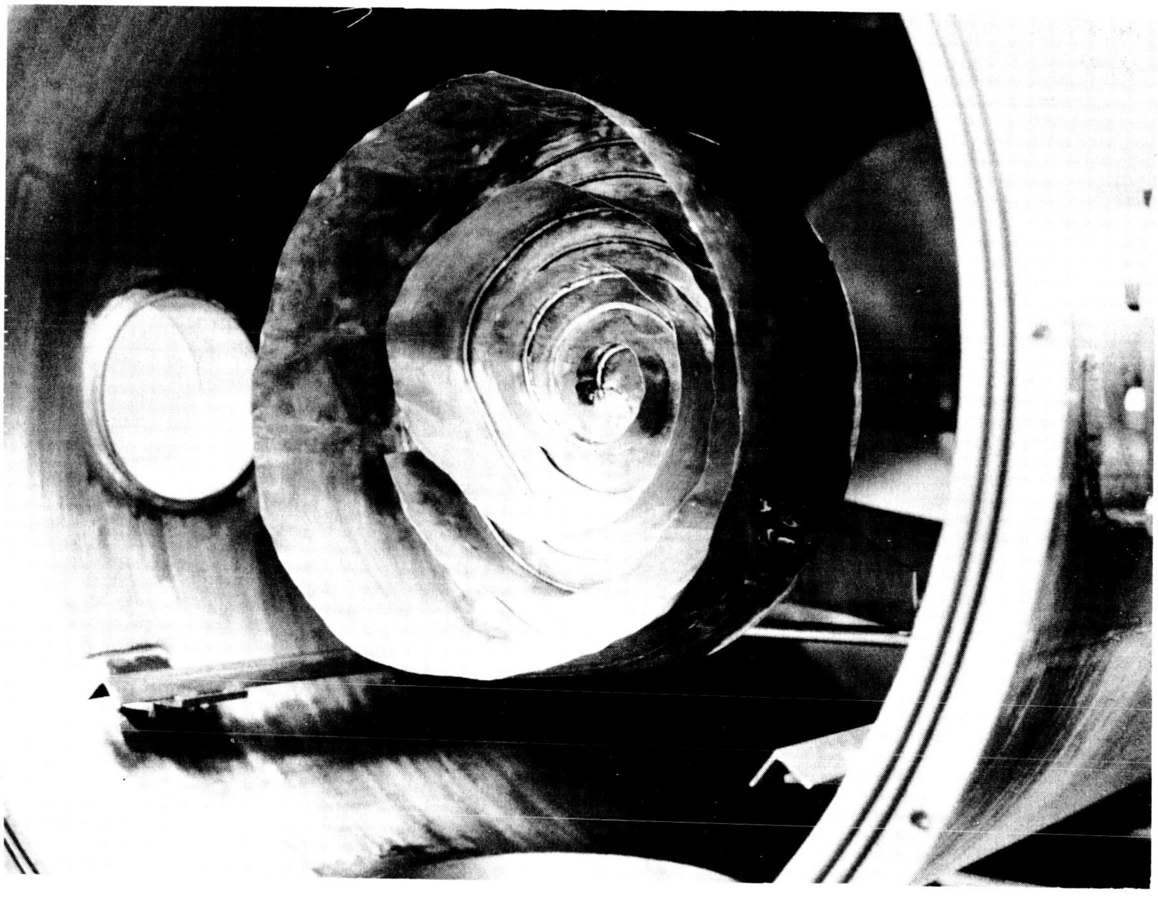

Figure 11. Total Calorimeter Mounted on Movable Base in Vacuum Tank

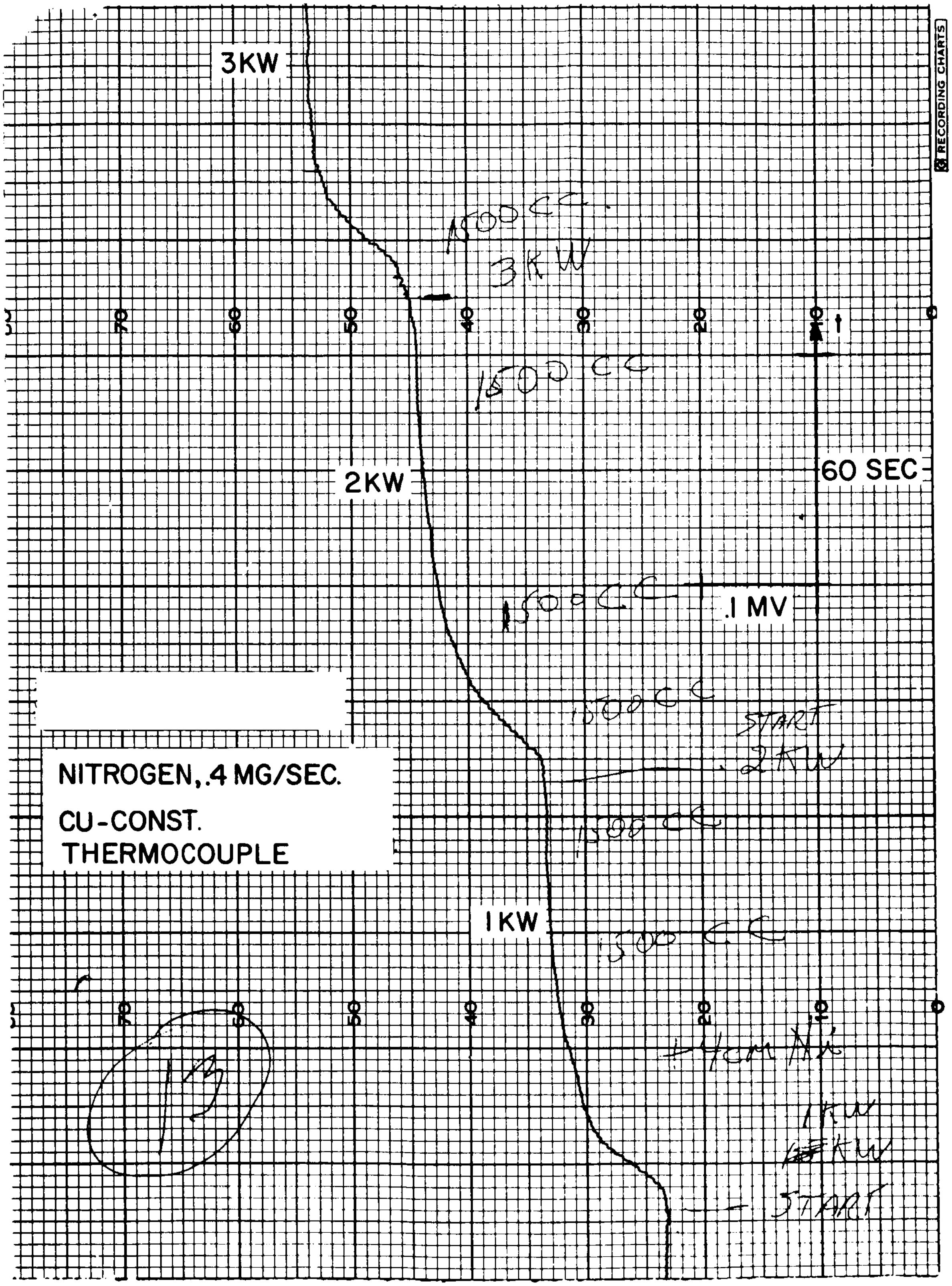

Figure 12. Typical Total Calorimeter Outlet Temperature Record During a Test; 1500 cc/min. Water Flow.

Figure 13. A 28-unit array of these probes is illustrated in Figure 14. The probe circuit is shown in Figure 15. These probes are identical to those developed during an earlier contract (see Final Report NAS3-3567).

Power density is measured by measuring the temperature rise of the collector cup during a test of known duration. Knowing the heat capacity of the collector, the time, and the temperature change allows calculation of the energy and the average power absorbed by the cup. The thermocouple leads from each probe pass through the vacuum wall at the central hub of the array. An ice-bath cold junction is employed, and a stepping switch is then used to connect the probe e.m.f.'s sequentially to a recording millivoltmeter (Photovolt "Microcord" Model 44). The temperature decay rate of each probe collector is sufficiently small so that all 28 temperatures can be recorded without any significant change in collector temperature taking place during the recording time.

Ion flux density is measured by biasing the collector strongly negative with respect to the enclosure and entrance grid so that all electrons are removed from the stream. The recorded collector current (through the copper thermocouple wire) then gives the ion arrival rate, and division by the probe entrance area (1.26 cm^2) yields ion flux density (ions/cm^2-sec). The gridded entrance causes approximately an 8% shadow but prevents the retarding field from extending out into the space beyond the probe and thereby increasing the effective ion collection area. The validity of this procedure was verified during NAS3-3567 studies, but these current measurements give rise to some doubt, as discussed in the experimental results section.

There are 16 microammeters so that ion currents to all sixteen probes can be measured simultaneously. Currents are recorded by taking a photograph of the 16-meter panel, as shown in the photographs of Figure 16. It can be noted from the data in Figure 16 that ion currents are taken for several (in this case three) collector bias voltages, and the saturation currents are interpreted from the resulting curves. Although only a few tenths of a volt

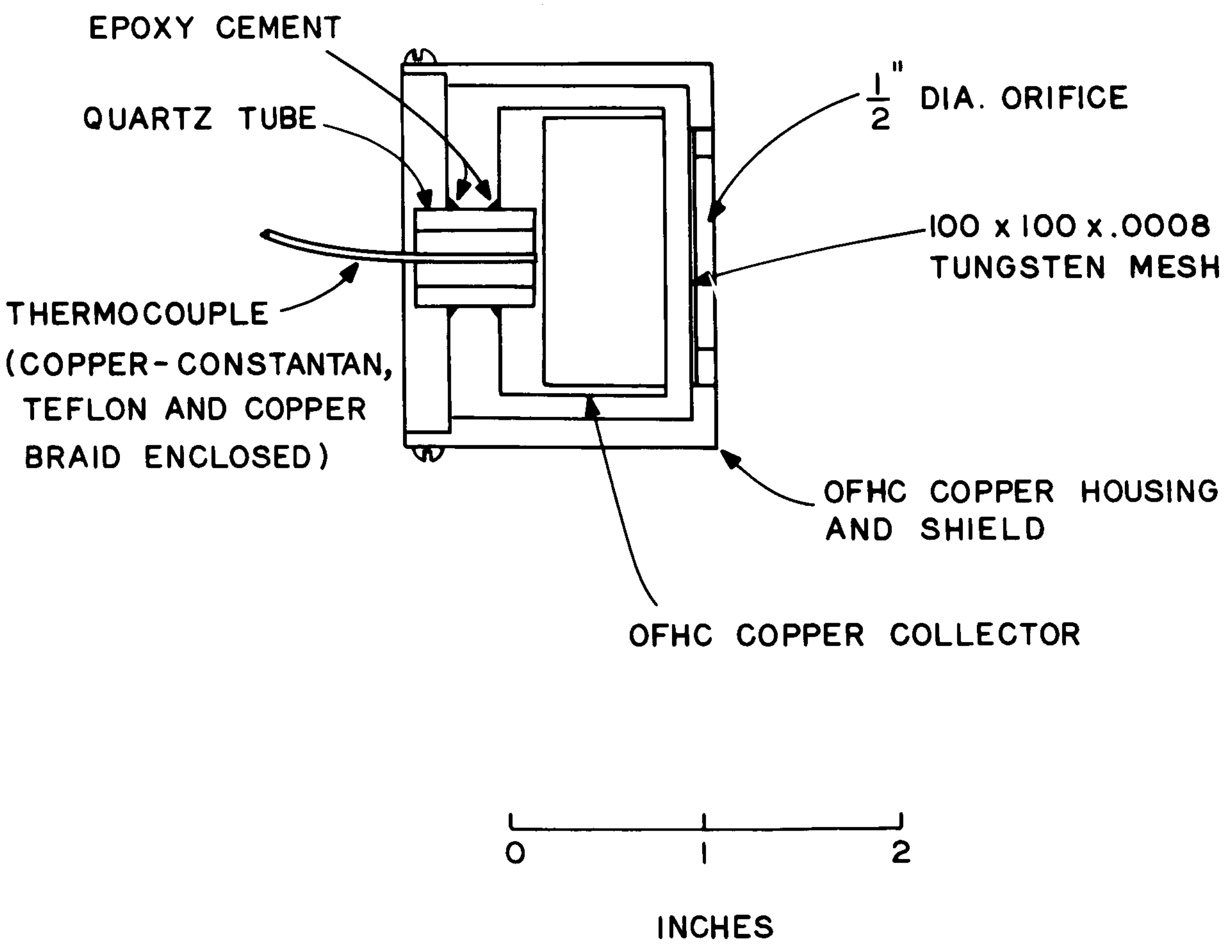

Figure 13. Diode Probe

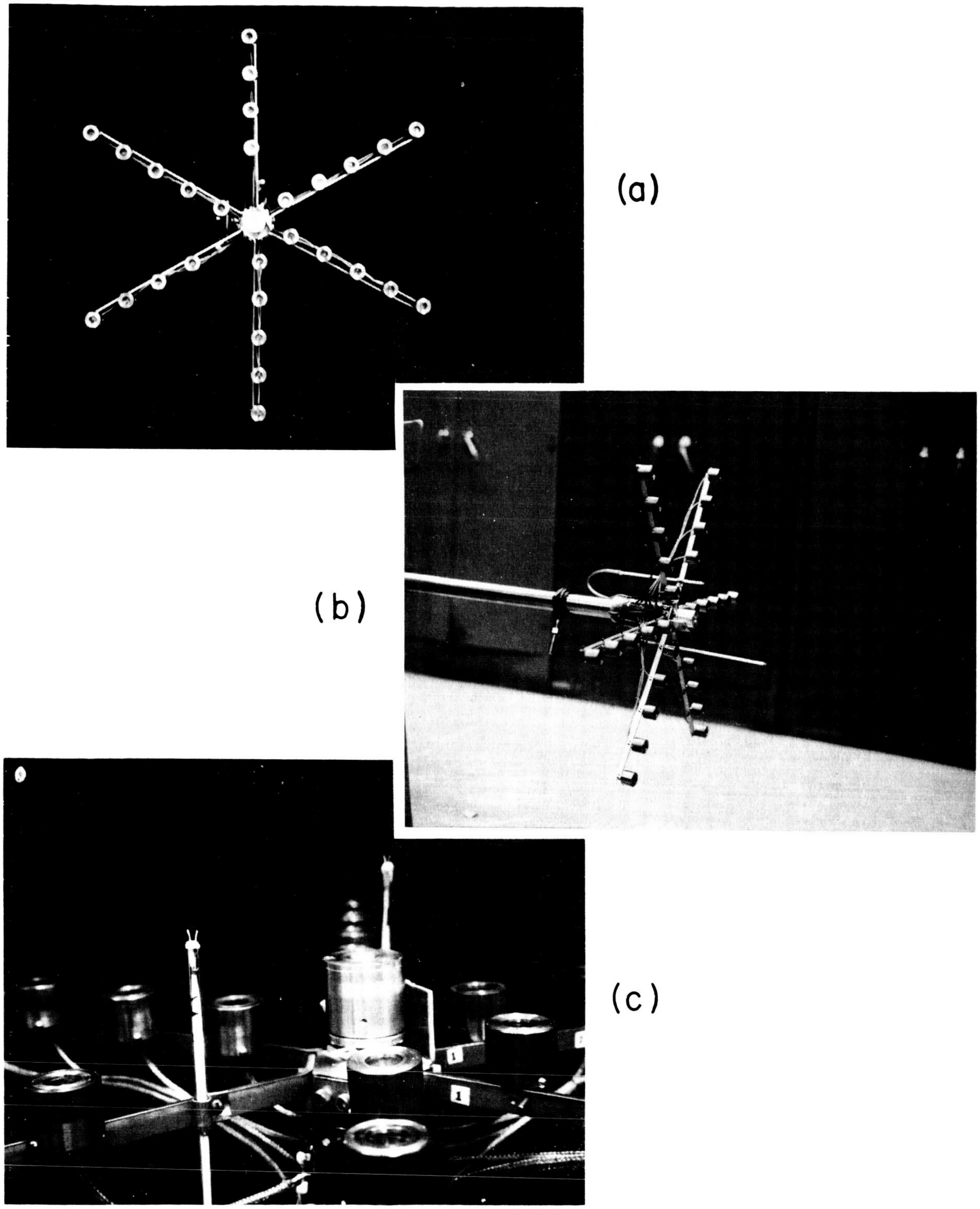

Figure 14. Multichannel Sampling-Probe Array
a. Frontal view, showing star pattern
b. Array mounted on support shaft
c. Close-up view, showing details of the velocity-analyser probe (on center), the potential probes (with emitting filaments at tips) and the diode (ion/power flux) probes.

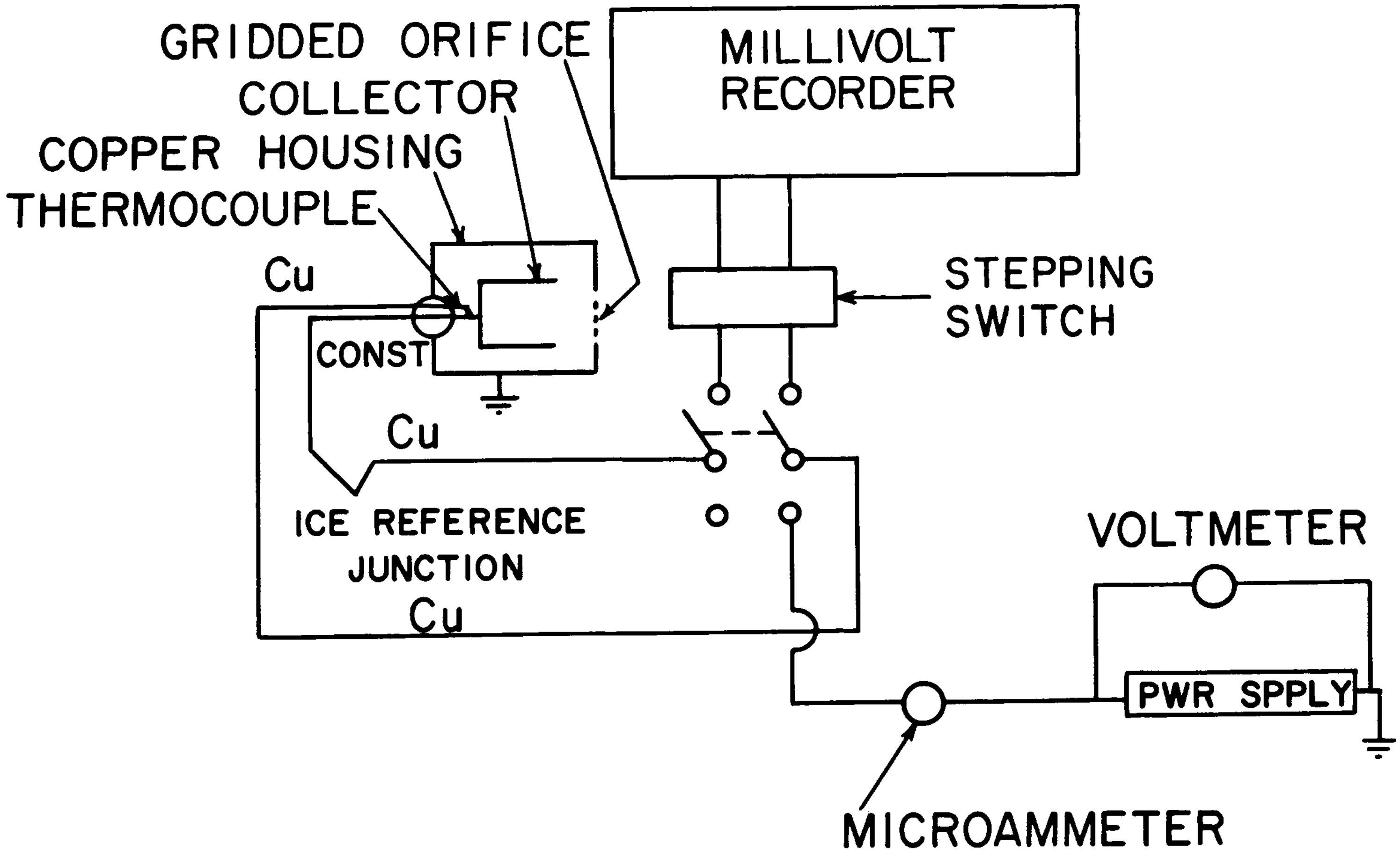

Figure 15. Sampling Probe Circuit (Typical of Sixteen)

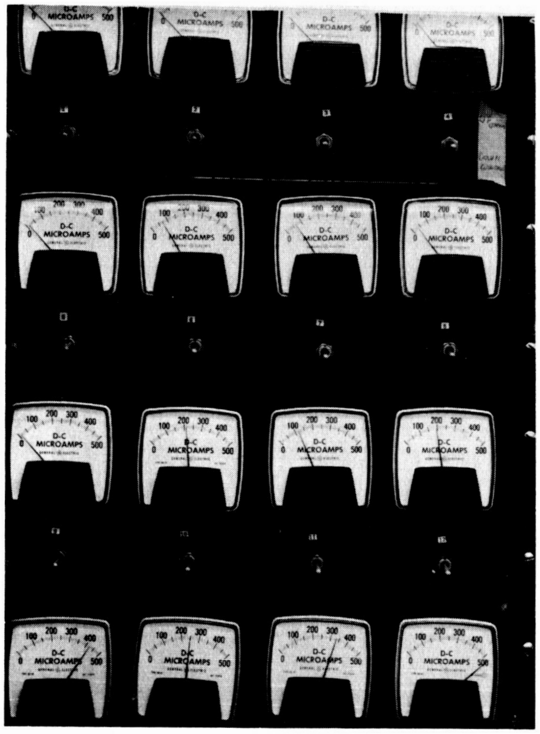

70v

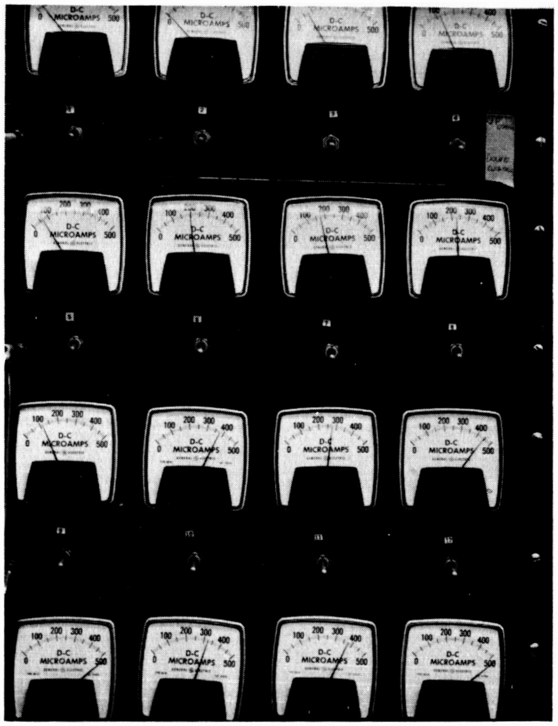

105v

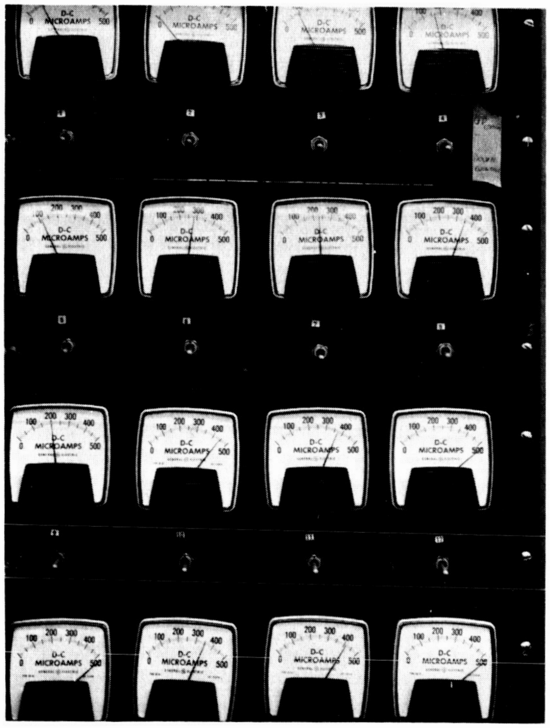

160v

Figure 16. Typical 16-Channel, Sampling Probe Data

should be needed to reflect the plasma electrons, it is seen that on the order of two hundred volts is needed to reach ion saturation current. This is explained by realizing that, after the electrons have been reflected, the probe acts as an ion diode and is space-charge limited, governed by the well-known Child-Langmuir relation. The large collector voltage is required to "pull across" to the collector all the ions arriving at the grid.

2.5.6 Potential Probe

The plasma potential probe consists of a heated emitting filament. If the probe current response curve near plasma potential is determined both with and without the probe emitting, the plasma potential presumably can be determined by either the "break" in the I-V curve or by the potential at which the emitting and non-emitting I-V curves (of the same probe) start to diverge. Here, I is probe current and V is probe bias voltage.

Since only relative probe currents are needed for the determination of plasma potential, the probe shape is not critical. Thus ordinary miniature light bulb filaments were used as a conveniently available source of emitting tungsten probes.

The plasma potential probes thus far used each consist of a GE #43 miniature lamp filament cemented to the end of a glass tube as shown in Figure 17. On testing several such filaments within an anode and in vacuum, they were found to give satisfactory life and 23-40 milliamps electron emission current at 75% filament overvoltage (4.4 volts AC).

Two of the above potential probes were mounted on the "multi-channel probe array" frame as shown in Figure 14. Both probes were mounted 7 cm from the center of the array, with the filament of one of them (probe A) being 2 cm ahead of the diode probes, and the filament of the other potential probe (probe B) being 8.5 cm ahead of the diode probes.

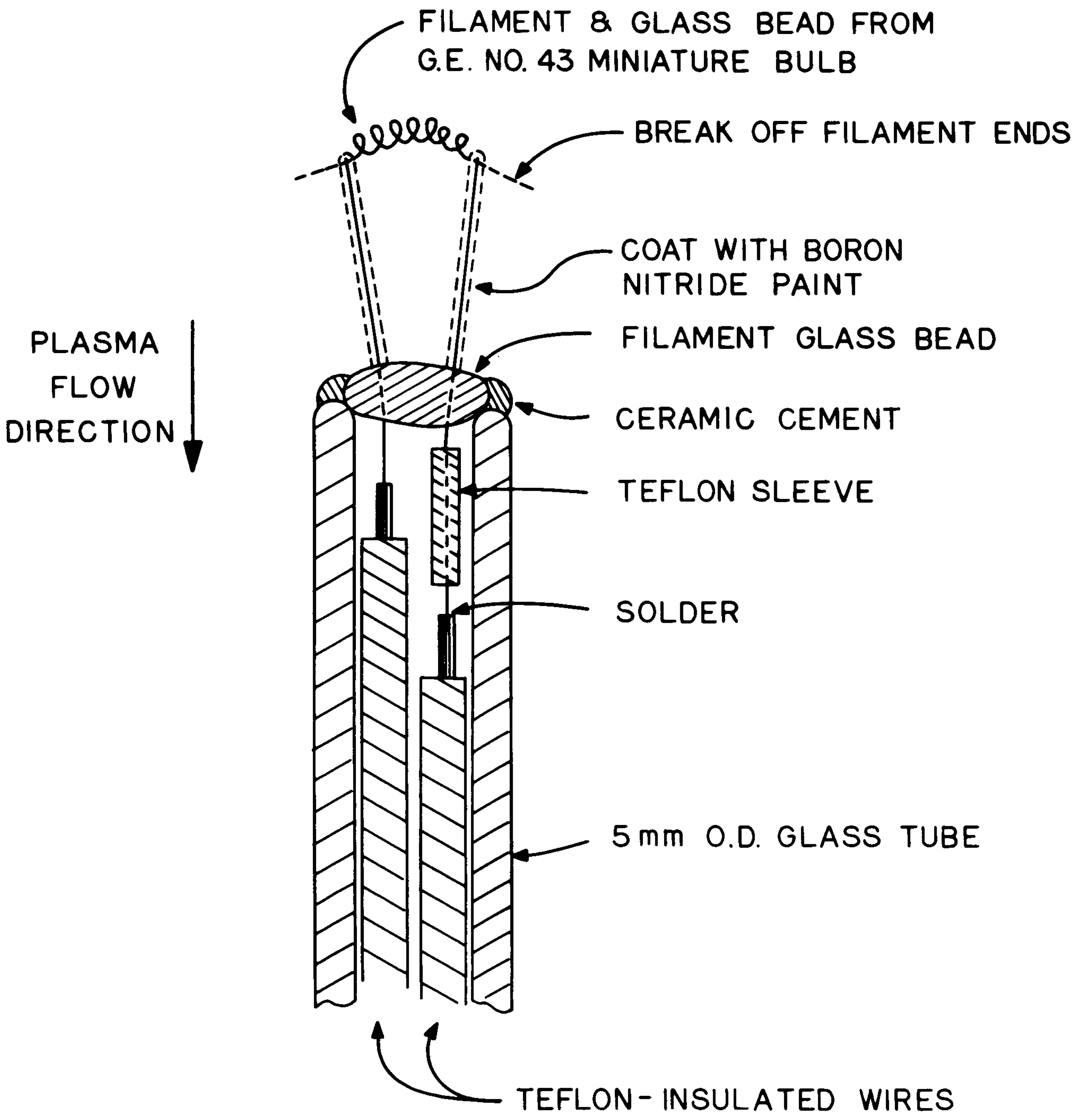

Figure 17. Emitting Plasma Potential Probe

2.5.7 Energy Analyser Probe

A two-gridded energy analysing probe has been constructed for determining ion velocities. As indicated in Figure 18 an inner ion collector plate is positively charged (variable) so as to collect only those ions above a certain energy, a grid adjacent to the above plate is negatively charged so as to repel all electrons, and an outer grid is at ground potential so as to limit the field from the negative grid.

Some earlier measurements[1] with a simple grid-less sampling probe indicated an exhaust ion current density of about 1.5 milliamps/cm^2. To successfully operate a multi-gridded ion velocity analysing probe with such a plasma, the probe must be designed so as to avoid space-charge limitations.

The Langmuir-Child equation[2] can be used to determine the spacecharge limited (i.e., maximum permitted) ion current through the negative grid to the positive collector: Assuming a monoenergetic beam of argon ions directed into the analysing probe, we find that the negative grid-positive collector spacing must be decreased to 0.09 cm (about 1/32 inch) and the collector-grid potential difference increased to 150 volts if the ion current limit is to be increased to 2.0 milliamps/cm^2.

Since it is difficult to reduce the grid-collector spacing to less than 1/32 inch without increasing the chances of forming grid ripples, touching, and shorting out, the analyser probe has grid-grid and grid-collector separations of 1/32 inch. Even maintaining the 1/32 inch spacings, the space-charge limitation can be further eased, if necessary, by increasing the negative grid potential. Also, the limited "transparency" of the grids will considerably reduce the actual ion current to the collector.

The use of simple flat collector plate results in the loss of some ion current due to the failure of a small fraction of the ions to neutralize before leaving the collector surface. This problem could be considerably reduced if the collector plate were replaced with a variably positive ion repelling grid followed by a negative (with respect to positive grid) ion collector plate.

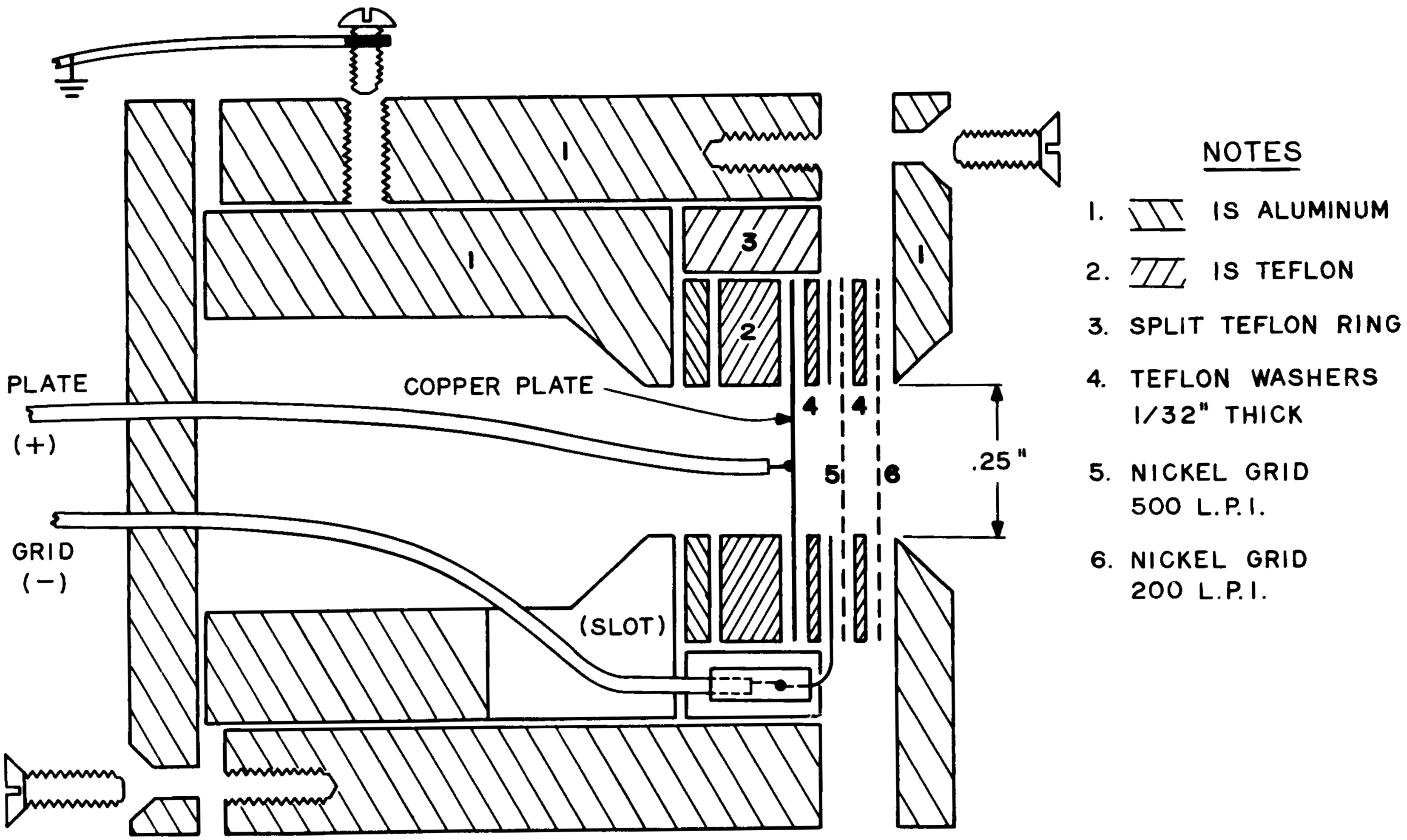

Figure 18. Energy Analysing Probe (Scale Enlarged 4:1)

With a negative plate-positive grid spacing of 0.09 cm it can be calculated[2] as above that a potential difference of 150 volts would be required for a space charge current limitation of 2.0 milliamps/cm^2. [A negative collector cup of significant depth is thus not reasonable since the space charge current limitation is universely proportional to the square of the positive grid - negative collector surface spacing[2].] Since such additional grids and potentials considerably increase the practical problems of probe operation and data recording with relatively little increase in data quality, the energy analysing probe has been constructed with a positive plate and no positive grid as discussed in the previous paragraph.

The ion energy analyser probe thus far used consists of a nickel 200 line per inch (l.p.i.) grounded grid, a nickel 500 l.p.i. negative (electron repelling) grid, and a positive ion selecting and collecting copper plate. The 200 and 500 l.p.i. grids are stated by the manufacturer to be 70% and 58% transparent, respectively. As shown in Figure 18, 1/32 inch thick Teflon washers separate the grids from each other and from the collector plate. Of the limited grid materials available, nickel has been initially employed because of its lower sputtering yield and higher melting point than copper. Similar copper grids are available for use if desired, as are grids with closer wire spacings.

The above energy analyser probe was mounted at the center of the "multichannel probe array" frame as shown in Figure 14. This probe was mounted such that its grounded grid was about 2.0 cm ahead of the diode probes and even with one of the potential probes.

2.5.8 Thrust Stand

A thrust stand for the cyclotron-resonance accelerator has been designed and ordered. An assembly drawing of this system is shown in Figure 19. Its features are dominated by the large rectangular pressure box, which houses the coil and accelerator. This enclosure was necessitated by the

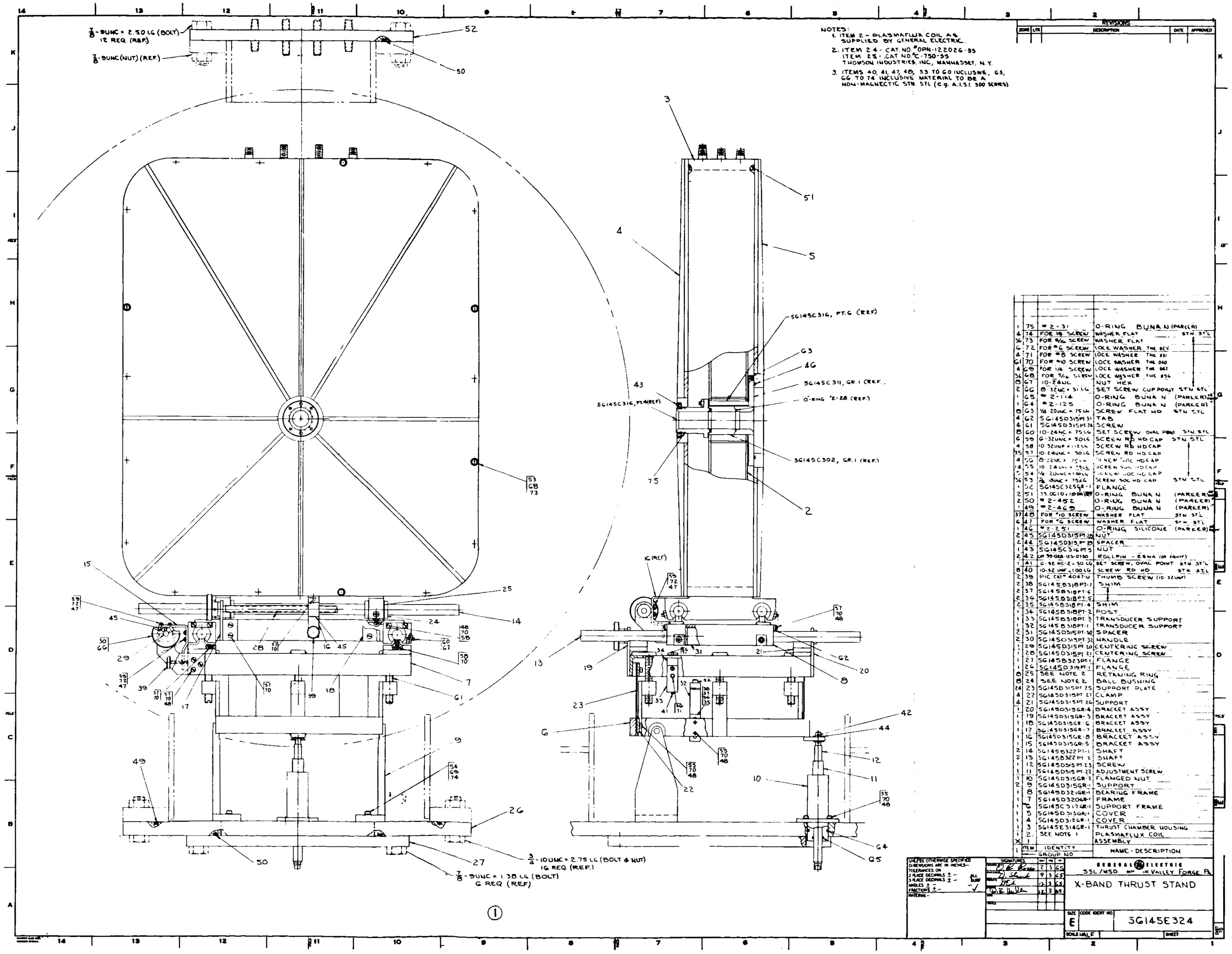

	ITEM	IDENTITY	NAME - DESCRIPTION	
1	75	#2-31	O-RING BUNA N (PARKER)	
4	74	FOR 1/4 SCREW	WASHER FLAT	STN. ST'L
36	73	FOR 5/16 SCREW	WASHER FLAT	
6	72	FOR #6 SCREW	LOCK WASHER THK .025	
4	71	FOR #8 SCREW	LOCK WASHER THK .031	
61	70	FOR #10 SCREW	LOCK WASHER THK .040	
4	69	FOR 1/4 SCREW	LOCK WASHER THK .047	
36	68	FOR 5/16 SCREW	LOCK WASHER THK .056	
8	67	10-24NC	NUT HEX	
2	66	8-32NC × .31 LG	SET SCREW CUP POINT	STN STL
1	65	#2-114	O-RING BUNA N	(PARKER)
1	64	#2-125	O-RING BUNA N	(PARKER)
8	63	1/4-20UNC × .75 LG	SCREW FLAT HD	STN STL
4	62	5G145D315PT-31	TAB	
4	61	5G145D315PT-24	SCREW	
8	60	10-24NC × .75 LG	SET SCREW OVAL POINT	STN. STL
6	59	6-32UNC × .50 LG	SCREW RD HD CAP	STN STL
4	58	10-32UNF × 1.12 LG	SCREW RD HD CAP	
35	57	10-24UNC × .50 LG	SCREW RD HD CAP	
4	56	8-32UNC × .75 LG	SCREW SOC HD CAP	
14	55	10-24UNC × .75 LG	SCREW SOC HD CAP	
5	54	1/4-20UNC × 1.00 LG	SCREW SOC HD CAP	
36	53	5/16-18UNC × .75 LG	SCREW SOC HD CAP	STN STL
1	52	5G145C325GR-1	FLANGE	
2	51	33.0G ID × .139 DIA	O-RING BUNA N	(PARKER)
2	50	#2-452	O-RING BUNA N	(PARKER)
1	49	#2-469	O-RING BUNA N	(PARKER)
37	48	FOR #10 SCREW	WASHER FLAT	STN ST'L
6	47	FOR #6 SCREW	WASHER FLAT	STN ST'L
1	46	#2-251	O-RING SILICONE	(PARKER)
2	45	5G145D315PT-28	NUT	
2	44	5G145D315PT-29	SPACER	
1	43	5G145C316PT-5	NUT	
2	42	CAT 99-028-125-0750	ROLLPIN - ESNA (OR EQUIV)	
1	41	6-32 NC-2 × .50 LG	SET SCREW, OVAL POINT	STN. ST'L
8	40	10-32 UNF × 1.00 LG	SCREW RD HD	STN. STL
2	39	PIC CAT# 4047-U	THUMB SCREW (10-32UNF)	
2	38	5G145B318PT-7	SHIM	
2	37	5G145B318PT-6		
2	36	5G145B318PT-5		
2	35	5G145B318PT-4	SHIM	
1	34	5G145B318PT-2	POST	
1	33	5G145B318PT-3	TRANSDUCER SUPPORT	
1	32	5G145B318PT-1	TRANSDUCER SUPPORT	
2	31	5G145D315PT-30	SPACER	
2	30	5G145D315PT-32	HANDLE	
1	29	5G145D315PT-20	CENTERING SCREW	
1	28	5G145D315PT-21	CENTERING SCREW	
1	27	5G145B323PT-1	FLANGE	
1	26	5G145D319PT-1	FLANGE	
8	25	SEE NOTE 2	RETANING RING	
8	24	SEE NOTE 2	BALL BUSHING	
24	23	5G145D315PT-25	SUPPORT PLATE	
4	22	5G145D315PT-27	CLAMP	
4	21	5G145D315PT-26	SUPPORT	
1	20	5G145D315GR-4	BRACKET ASSY	
1	19	5G145D315GR-3	BRACKET ASSY	
1	18	5G145D315GR-6	BRACKET ASSY	
1	17	5G145D315GR-7	BRACKET ASSY	
1	16	5G145D315GR-8	BRACKET ASSY	
1	15	5G145D315GR-5	BRACKET ASSY	
2	14	5G145B322PT-1	SHAFT	
2	13	5G145B322PT-2	SHAFT	
1	12	5G145D315PT-23	SCREW	
1	11	5G145D315PT-22	ADJUSTMENT SCREW	
1	10	5G145D315GR-2	FLANGED NUT	
2	9	5G145D315GR-1	SUPPORT	
1	8	5G145D321GR-1	BEARING FRAME	
1	7	5G145D320GR-1	FRAME	
1	6	5G145C317GR-1	SUPPORT FRAME	
1	5	5G145D313GR-1	COVER	
1	4	5G145D312GR-1	COVER	
1	3	5G145E314GR-1	THRUST CHAMBER HOUSING	
1	2.	SEE NOTE 1	PLASMAFLUX COIL	
X	1		ASSEMBLY	
1 ← GROUP NO	ITEM	IDENTITY	NAME - DESCRIPTION	

Figure 19. Thrust stand assembly drawing.

inability of the coil to operate in vacuum. The stand itself, below the box, consists primarily of positioning tracks for initial and final balancing of the stand. Four thin flexible legs (parts #23) support the stand and will be sufficiently loaded so that slight horizontal thrusts will cause appreciable bending of these legs. A linear motion transducer (supported by part #33) provides an electrical signal proportional to the displacement.

Electrical power, coolant water and propellant gas will be provided through the overhead couplings. Calibration will be carried out by noting the deflection resulting from a known axial force.

2.5.9 Microwave Probe

A microwave probing signal has been considered for use in measuring the electron density profile in the r-f/plasma interaction region, as described in the following paragraphs.

The wave equation governs the propagation of an electromagnetic wave through a plasma. For a wave of the form;

$$E = E_o \exp j(\omega t - kz) \tag{1}$$

the wave equation may be written:

$$\frac{d^2 E}{dx^2} + k^2 E = 0. \tag{2}$$

The propagation constant k for a right-hand circularly polarized wave may be derived from the equation of motion of an electron giving

$$k^2 = \left(\frac{\omega}{c}\right)^2 \left\{ 1 - \left(\frac{\omega_p}{\omega}\right)^2 \left[\frac{1}{1 - \frac{\omega_c}{\omega} - j\,\nu/\omega} \right] \right\} \tag{3}$$

where ν is the collision frequency, ω_c is the electron cyclotron frequency and ω_p is the plasma frequency.

A reasonable approximation to the electron density distribution in the r-f/plasma boundary region is given by:

$$\eta = \eta_\infty (1 - e^{-\gamma \xi}) \tag{4}$$

where η is the electron density (electrons per cubic meter), η_∞ is the asymptotic electron density deep inside the plasma, ξ is the axial coordinate (in units of the free space wavelength), and γ is the space degradation coefficient.

The reflection coefficient can be obtained from a numerical solution to Equation (2), incorporating Equations (3) and (4), in the manner of Yen[3], who carried out a similar analysis for $\omega_c = 0$. These equations could be programmed for computer solution of the complex reflection coefficient R (ω) as a function of frequency for various ω_p, ω_c, ν, and γ conditions.

Since this absorption will take place within waveguide boundaries, the plane wave situation for which the Yen analysis holds will not be valid, and waveguide impedance procedures may be the most convenient approach. A procedure in which the true boundary is broken into a number of segments[4] should also be evaluated as a possibly easier and better method.

In order to use this microwave probe technique, measurement of the reflection coefficient as a function of frequency would be required in order to compare with the theory. This would necessitate in particular a variable frequency oscillator as well as a diplexer to launch and recover this low power probing frequency in the presence of the high-power 8350 mc wave.

3. EXPERIMENTAL RESULTS

3.1 Mark IV-L Accelerator (Axial-injection, long version)

A photograph of the Mark IV-L exhaust stream is shown in Figure 20. If the reasonable assumption is made that the luminous region indicates the approximate limits of the accelerated stream, then this illustration indicates that the plasma does not "fountain" back following the solenoidal field lines, although it does appear to continue spreading to some extent after leaving the engine. Quantitative measurements on the Mark IV-L accelerator are presented in Figures 21 - 26.

We note from Figure 21 that the reflection coefficient is very low (< 5%). This, of course, is a result of tuning, so that the plasma load is matched to the source; if tuning were to be carred out at each test, the reflection coefficient could in all instances be kept essentially zero. The r-f probe curves do not lend themselves to easy interpretation; undoubtedly the fact that the plasma probably has a cone shape, expanding away from the injection point, with propagation in the annular region between the cone and the waveguide wall, has much to do with the characteristics of these signals. In addition, a reasonably complex probe signal pattern is to be expected since these probes are indicative of the reasonably complex standing wave pattern which must exist within the accelerator. These probe signals with plasma are stronger than in the absence of plasma, probably due to both the annular propagation and standing wave effects. An additional point of interest is that one might have expected to have seen more clearly the enhancement of propagation with increased magnetic field strength, as predicted theoretically and as obtained in similar measurements on the Mark I accelerator during the NAS3-3567 studies.

The wall calorimeter temperatures indicated in Figure 22 exhibit the expected inverse relationship between the magnetic field strength and wall loss. For these calorimeters, the rate of heat lost is such that they rapidly reach an equilibrium temperature, and power received is a function of calorimeter equilibrium temperature, as was explained in section 2.5.3. Using

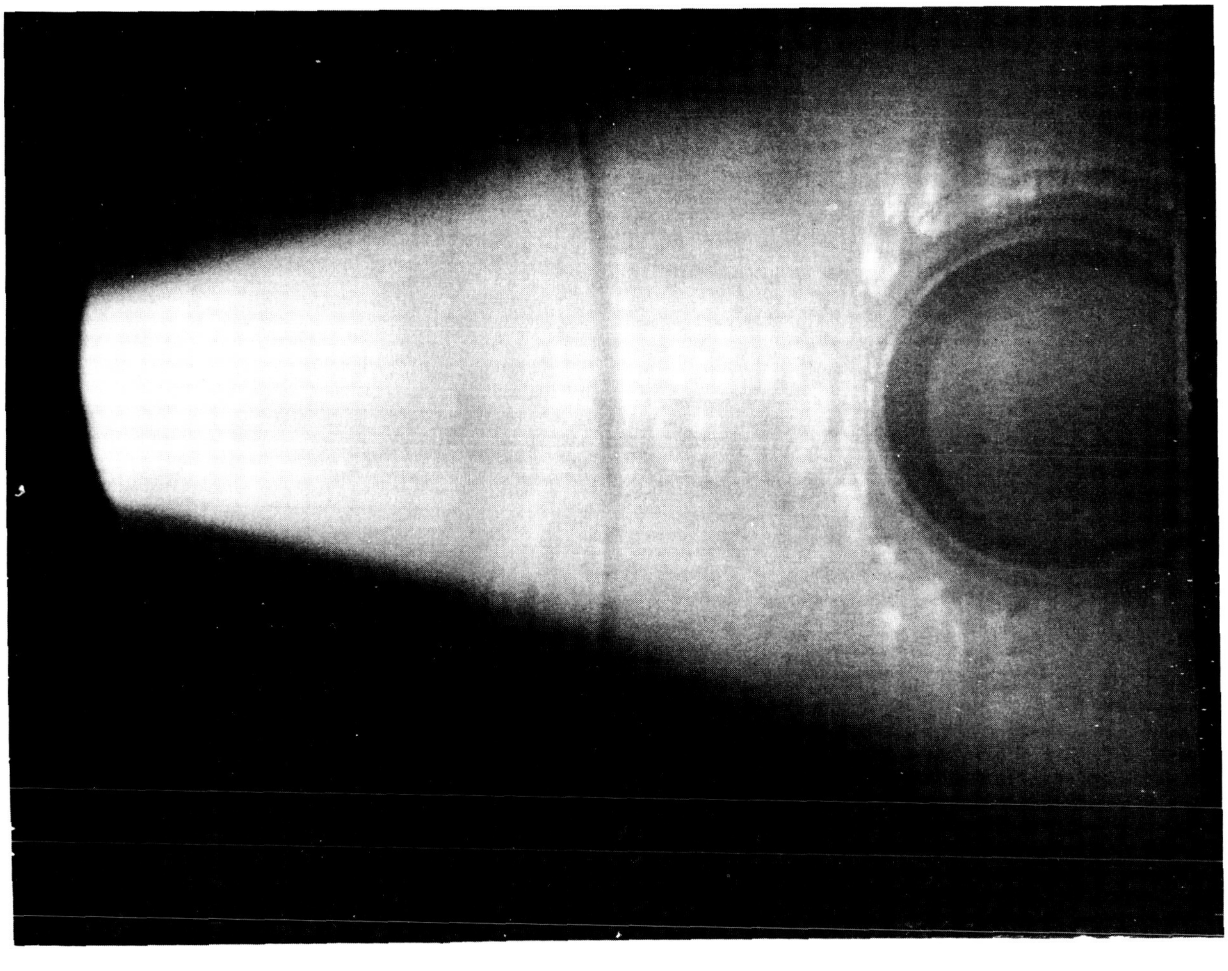

Figure 20. Exhaust Stream Emerging from Mark IV-L Accelerator (on the left) and Impinging on Calorimetric Collector (on the right), Argon, 2 kw, 5×10^{-5} torr Background Pressure.

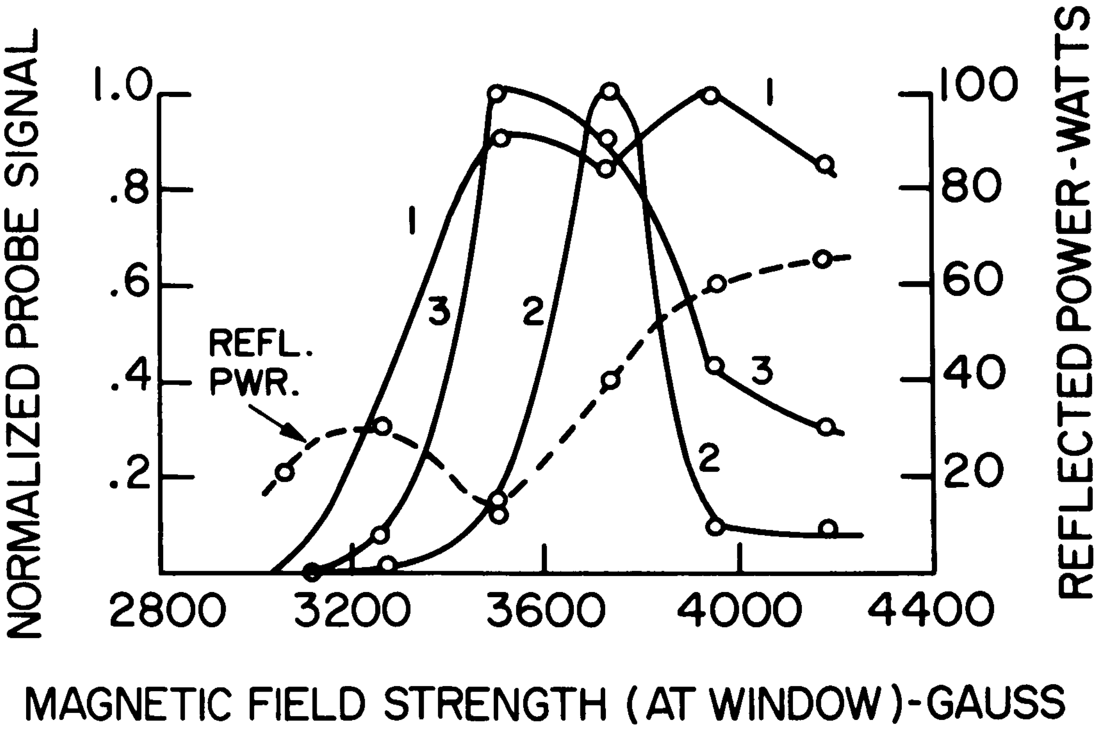

Figure 21. Dependencies of Reflected Power and R-F Antenna Probe Signals on Magnetic Field Strength. Nitrogen; .4 mg/sec, 2 kw R-F Power, Mark IV-L Acceleration

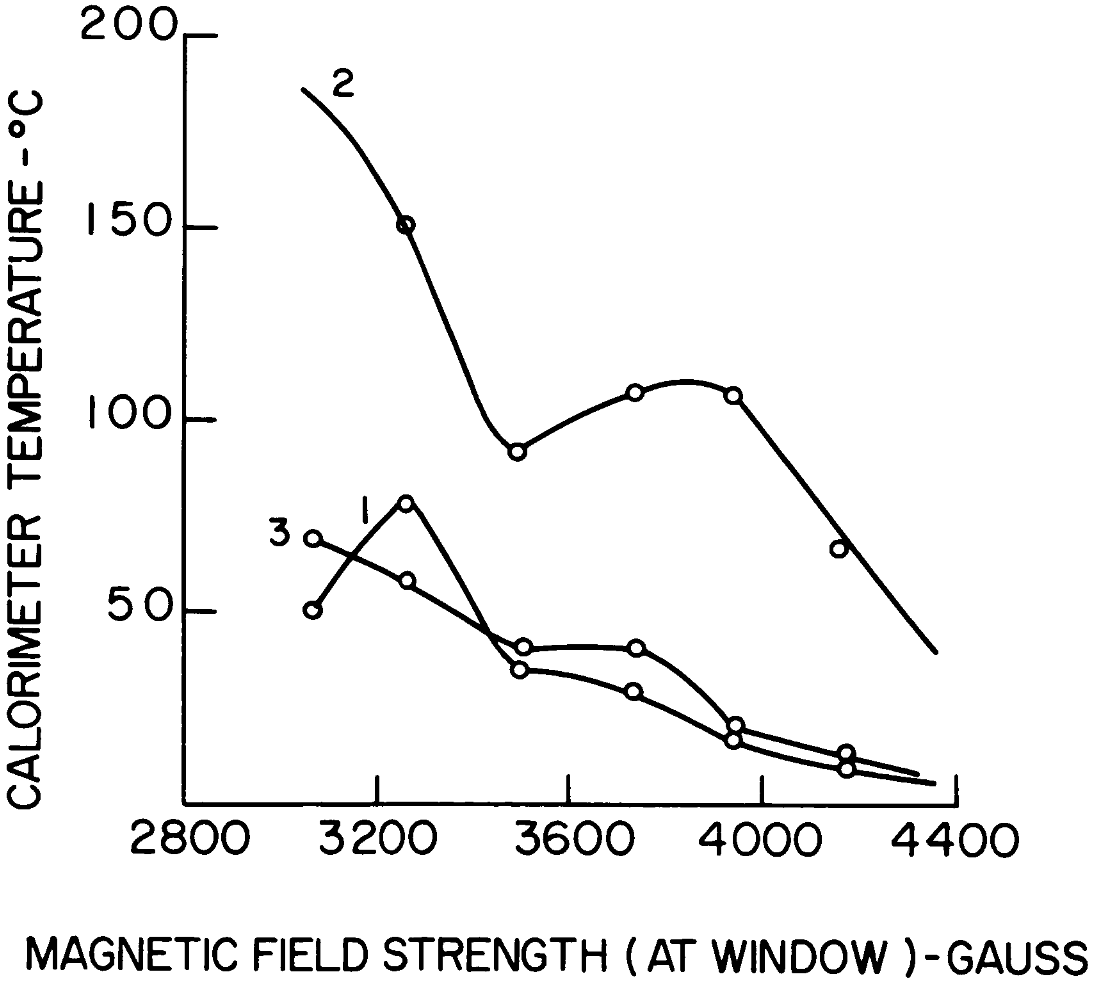

Figure 22. Dependencies of Wall Calorimeter Temperatures on Magnetic Field Strength. Nitrogen, .4 mg/sec, 2 kw RF Power, Mark IV-L Accelerator

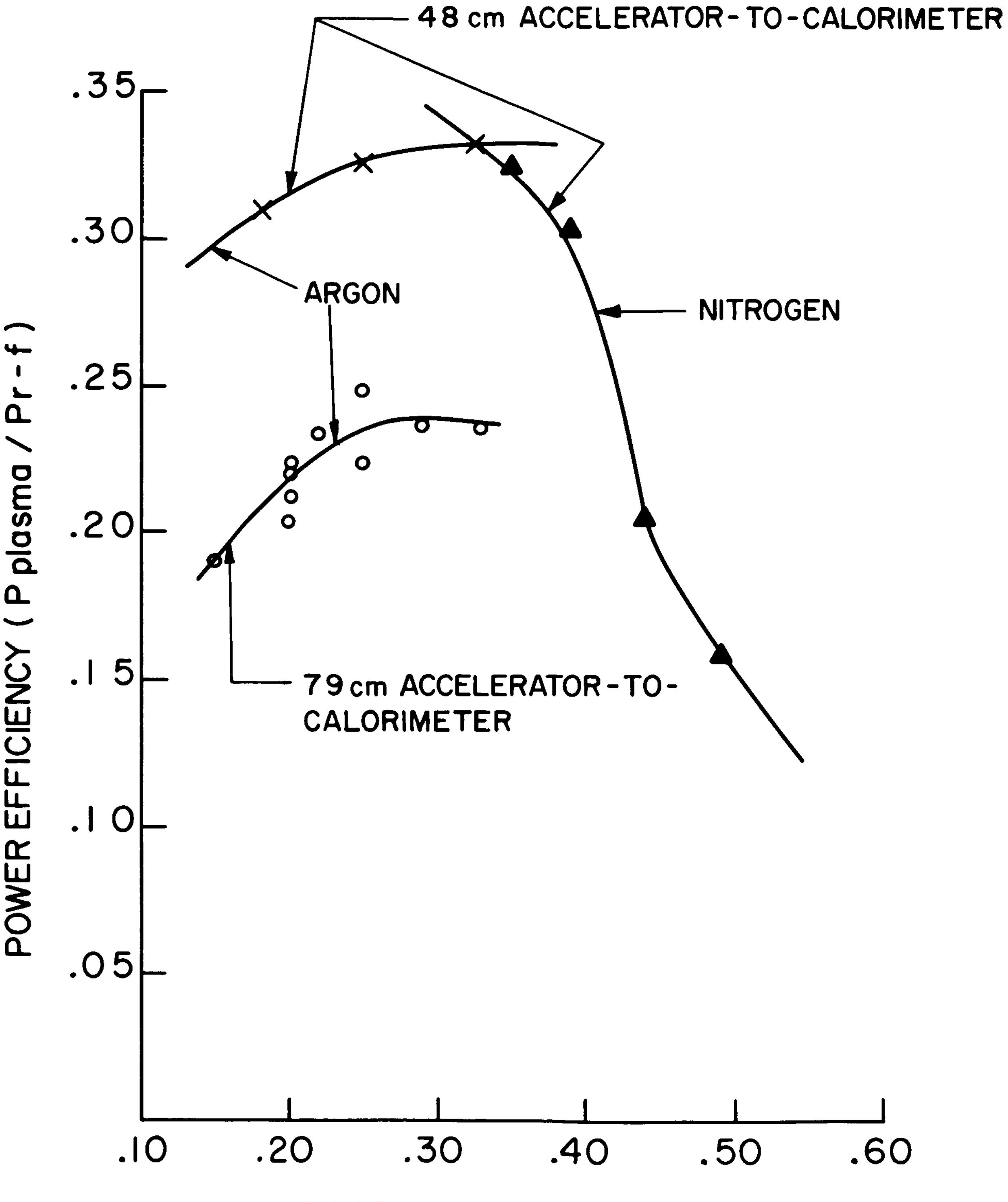

Figure 23. Dependence of Power Efficiency on Propellant Flow Rate, Propellant Species and Calorimeter Position, Mark IV-L Accelerator

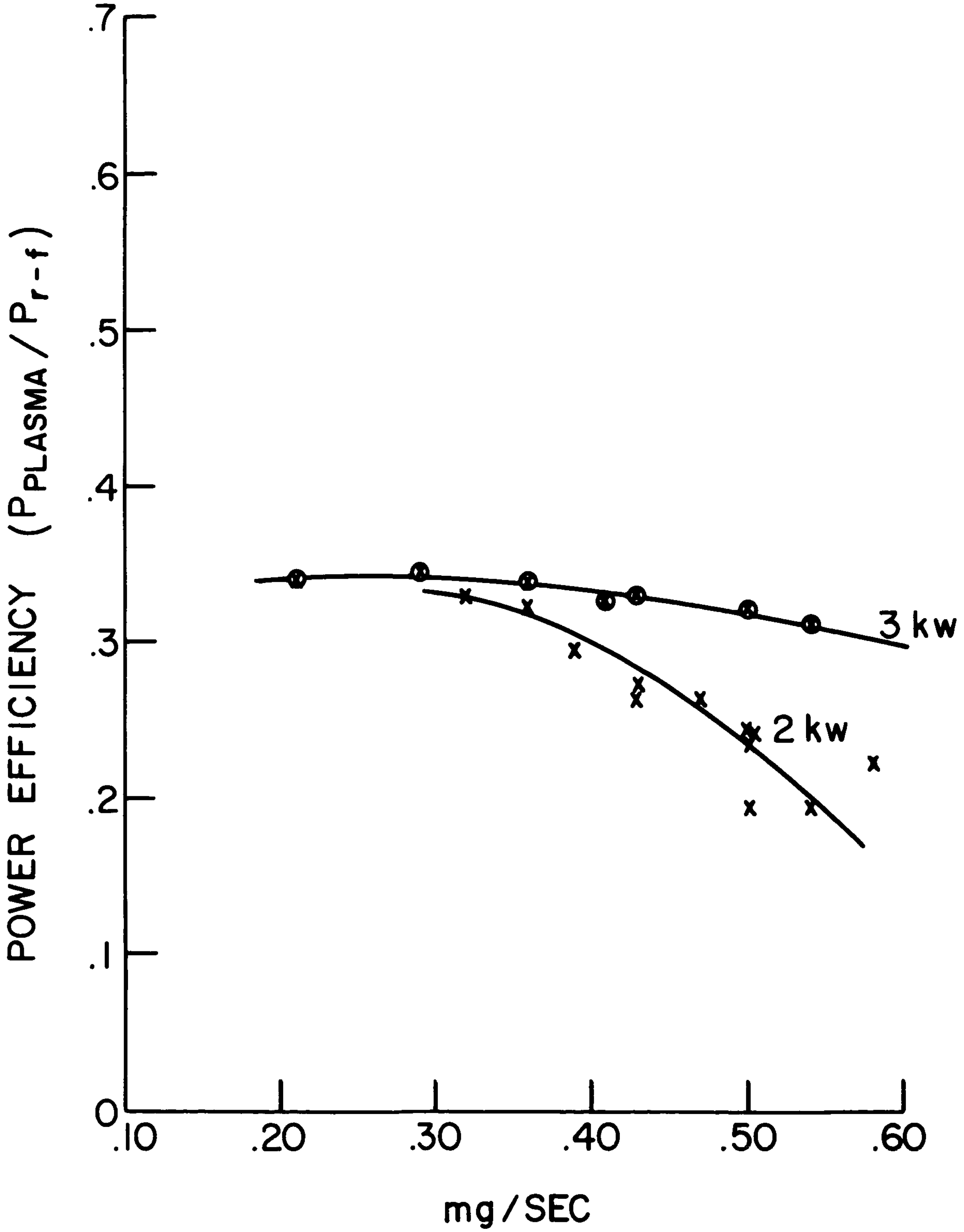

Figure 24. Dependence of Power Efficiency on Mass Flow Rate, Nitrogen, 3730 Gauss Window Magnetic Field Strength, Accelerator-to-Calorimeter Distance 33 cm Mark IV-L Accelerator

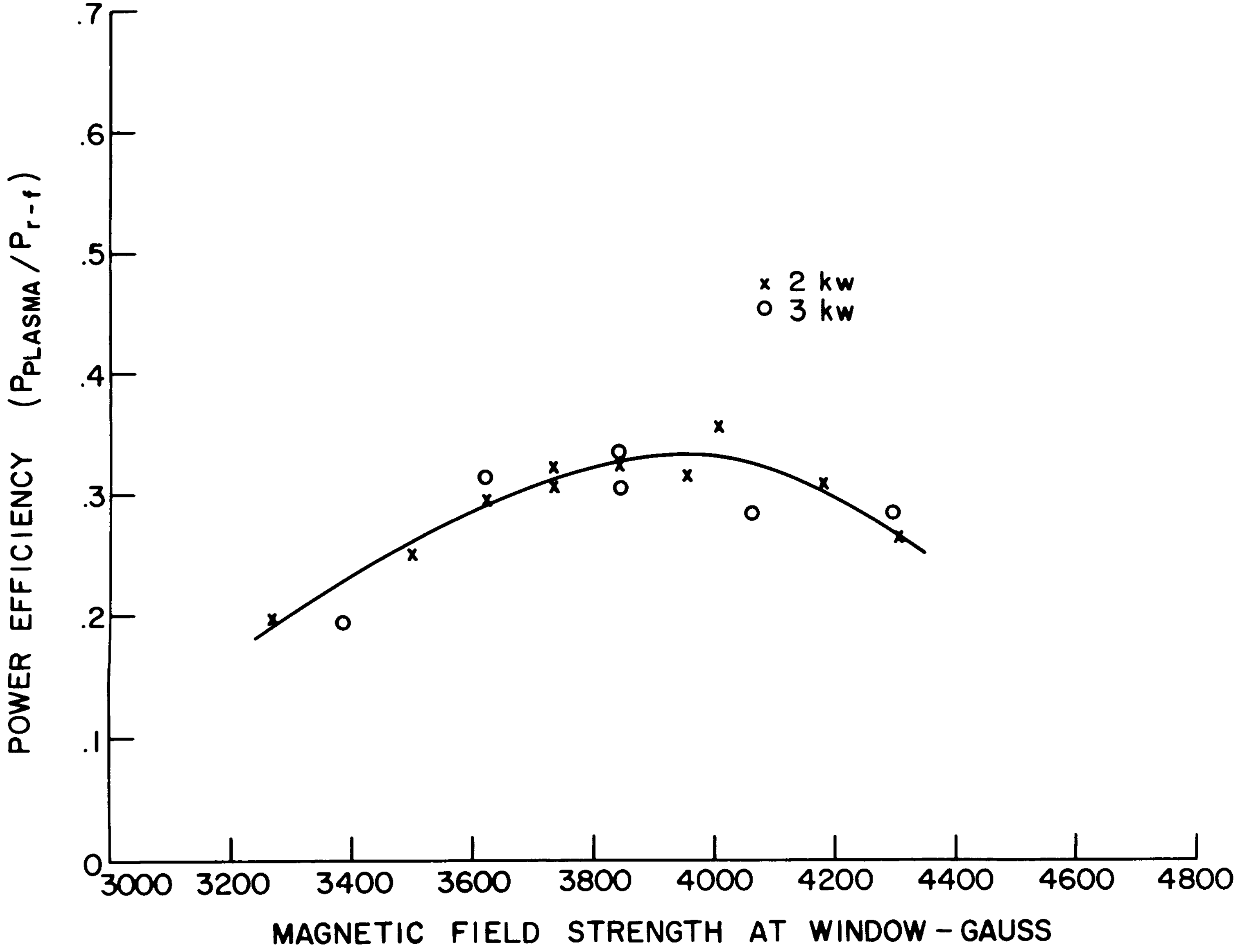

Figure 25. Dependence of Power Efficiency on Magnetic Field Strength, Nitrogen, .36 mg/sec, Accelerator-to-Calorimeter Distance 33 cm, Mark IV-L Accelerator

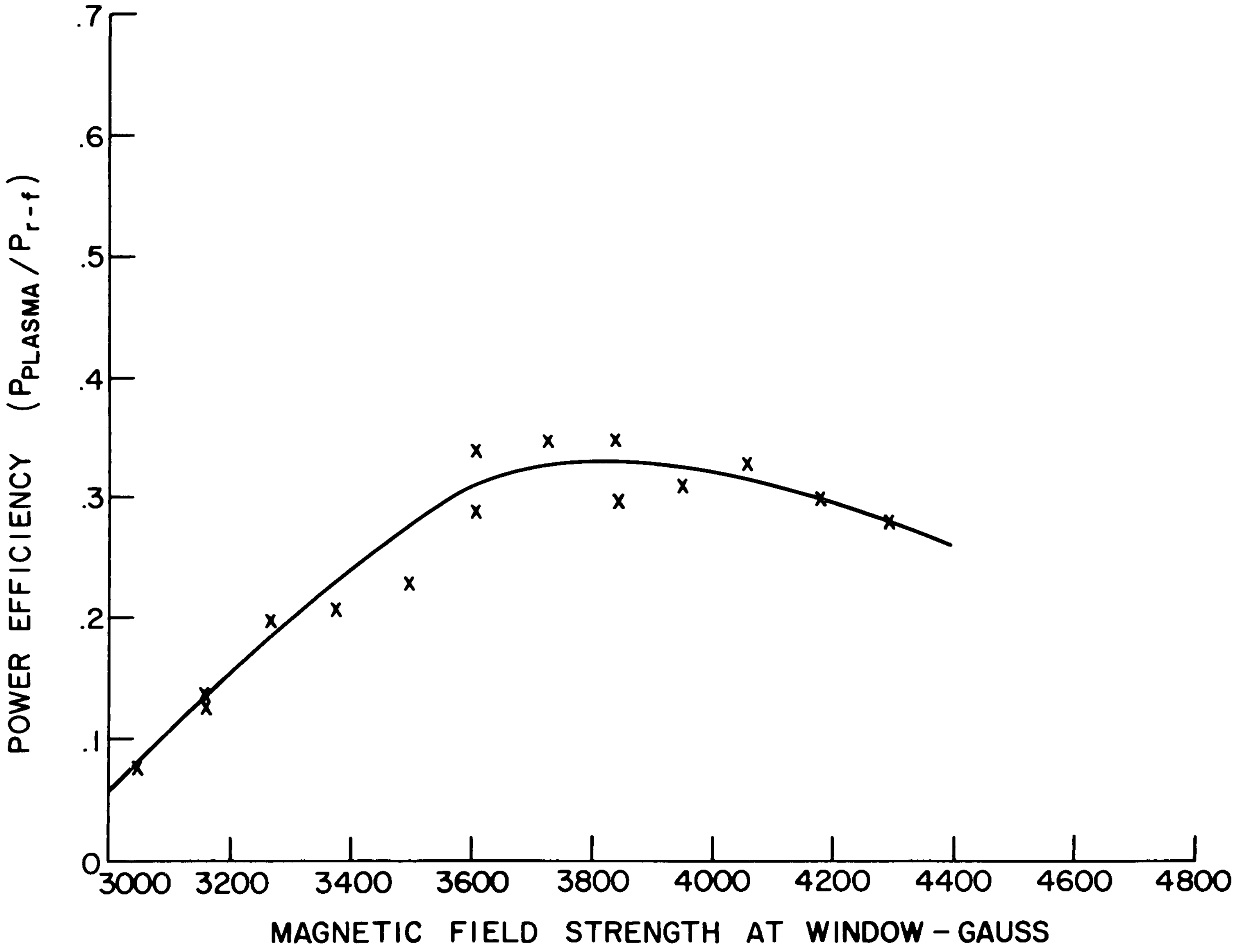

Figure 26. Dependence of Power Efficiency on Magnetic Field Strength, Argon, .19 - .22 mg/sec, Accelerator-to-Calorimeter Distance 33 cm. 2 kw. Mark IV-L Accelerator

the 1.3 watt/degree figure stated in section 2.5.3 yields wall power loss of perhaps 100-150 watts at low fields, decreasing to less than half of this at the higher field strengths. Inspection of the engine after several days testing ($\sim 10^4$ seconds operating time) revealed that the copper wall of the plasma chamber had suffered considerable erosion, with eroded copper (~0.19 gm) being redeposited on the face of the engine flange. Undoubtedly this erosion took place most severely during those tests conducted at low fields.

Total calorimeter power efficiency measurements are shown in Figures 23 - 26. The following items are interpreted from these curves:

1. There is an optimum mass flow rate for maximum efficiency (Figures 23 and 24).
2. At high flow rates (> optimum) the efficiency holds up better at higher power due possibly to frozen flow effects (Figure 24).
3. There is an optimum field for maximum efficiency (Figures 25 and 26).
4. This optimum field is considerably above resonance at the window. Plasma diamagnetism could contribute to this effect. The decrease in wall loss with increasing field (Figure 22) would also aid in achieving this result.
5. The optimum field is approximately independent of power (Figure 25) but appears to occur at a higher value with nitrogen than with argon.
6. The best power efficiency for the Mark IV-L accelerator is approximately 35%, with this same peak achieved in both argon and nitrogen.

More extensive testing of the Mark IV-L accelerator could have been carried out, but the poor power efficiency and the severe wall erosion suggested that time would be better spent investigating other geometries.

3.2 Mark IV-S Accelerator (Axial-injection, short version)

The Mark IV-S exhaust stream photograph (Figure 27) reveals that shortening the accelerator has not grossly diminished the collimation of the plasma jet. Power efficiency data are presented in Figures 28 - 32.

Figure 27. Exhaust Stream Emerging fromMark IV S Accelerator, Nitrogen, 2 kw, 1×10^{-5} Torr Background Pressure

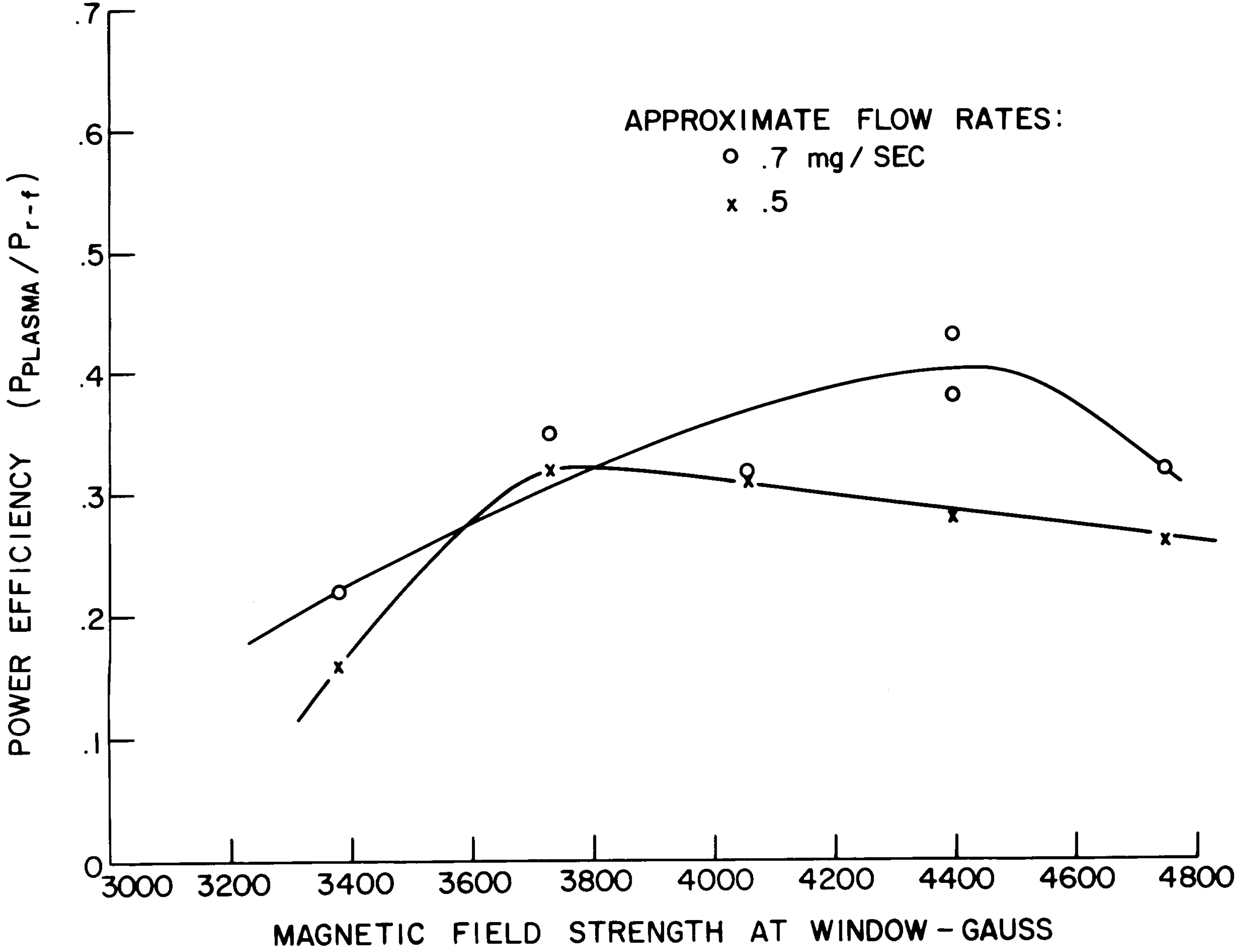

Figure 28. Dependence of Power Efficiency on Magnetic Field Strength, Krypton, 2 kw, Accelerator-to-Calorimeter Distance 43 cm, #B4 Beryllium Oxide Half-wavelength Window. Mark IV-S Accelerator

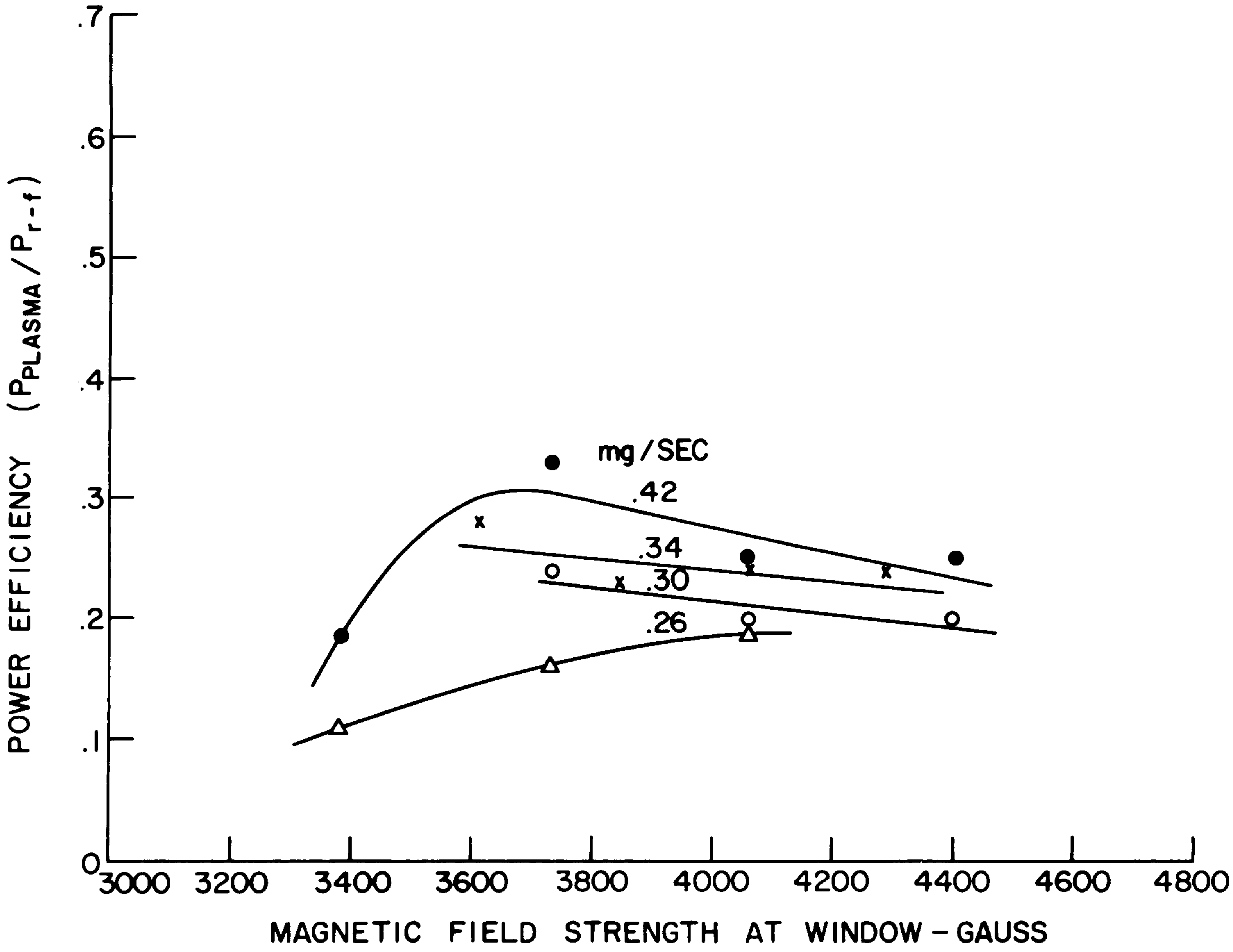

Figure 29. Dependence of Power Efficiency on Magnetic Field Strength, Nitrogen, 2 kw, Accelerator-to-Calorimeter Distance 43 cm, #B5 Beryllium Oxide Half-wavelength Window, Mark IV-S Accelerator

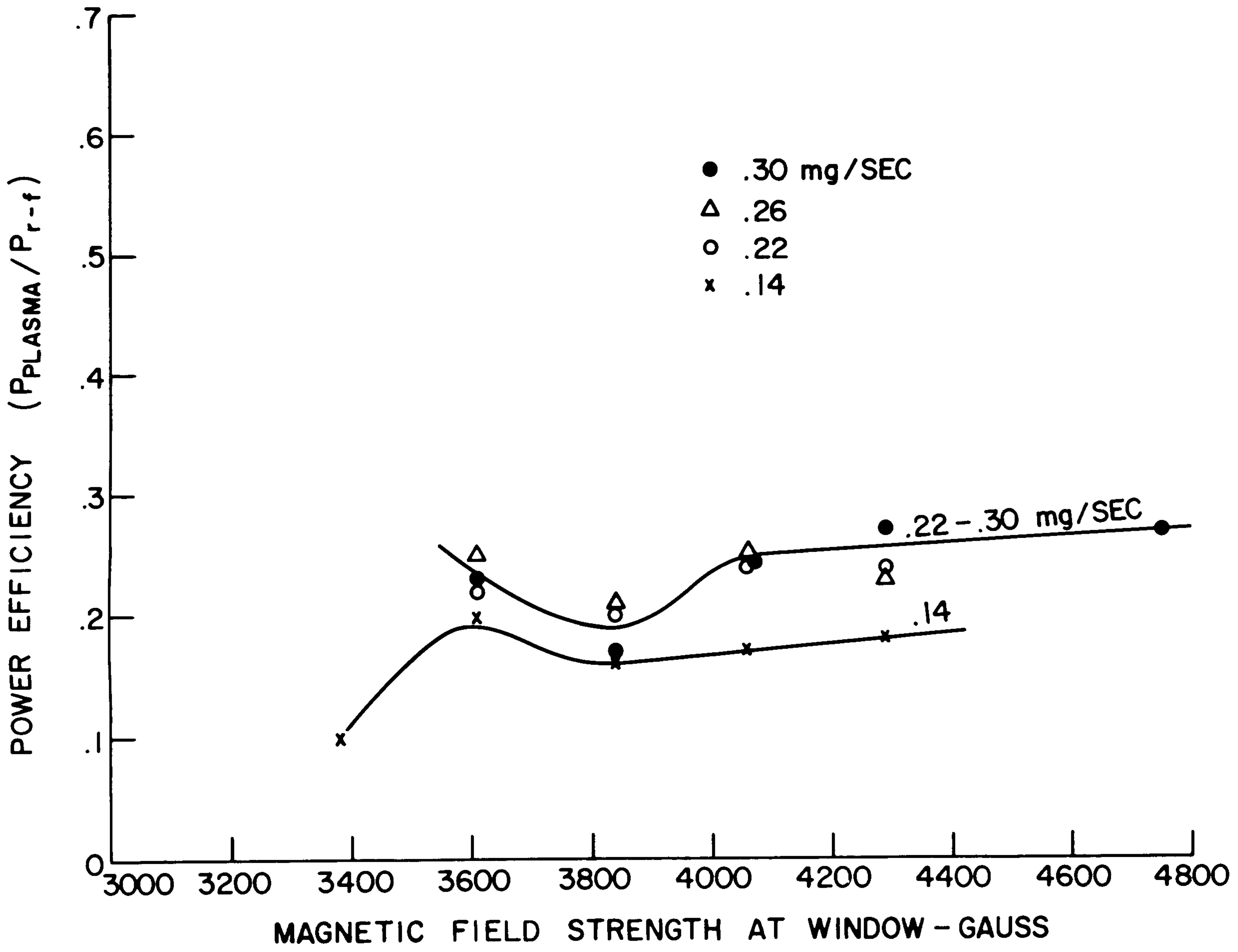

Figure 30. Dependence of Power Efficiency on Magnetic Field Strength, Argon, 2 kw, Accelerator-to-Calorimeter Distance 43 cm, #B5 Beryllium Oxide Half-wavelength Window, Mark IV-S Accelerator

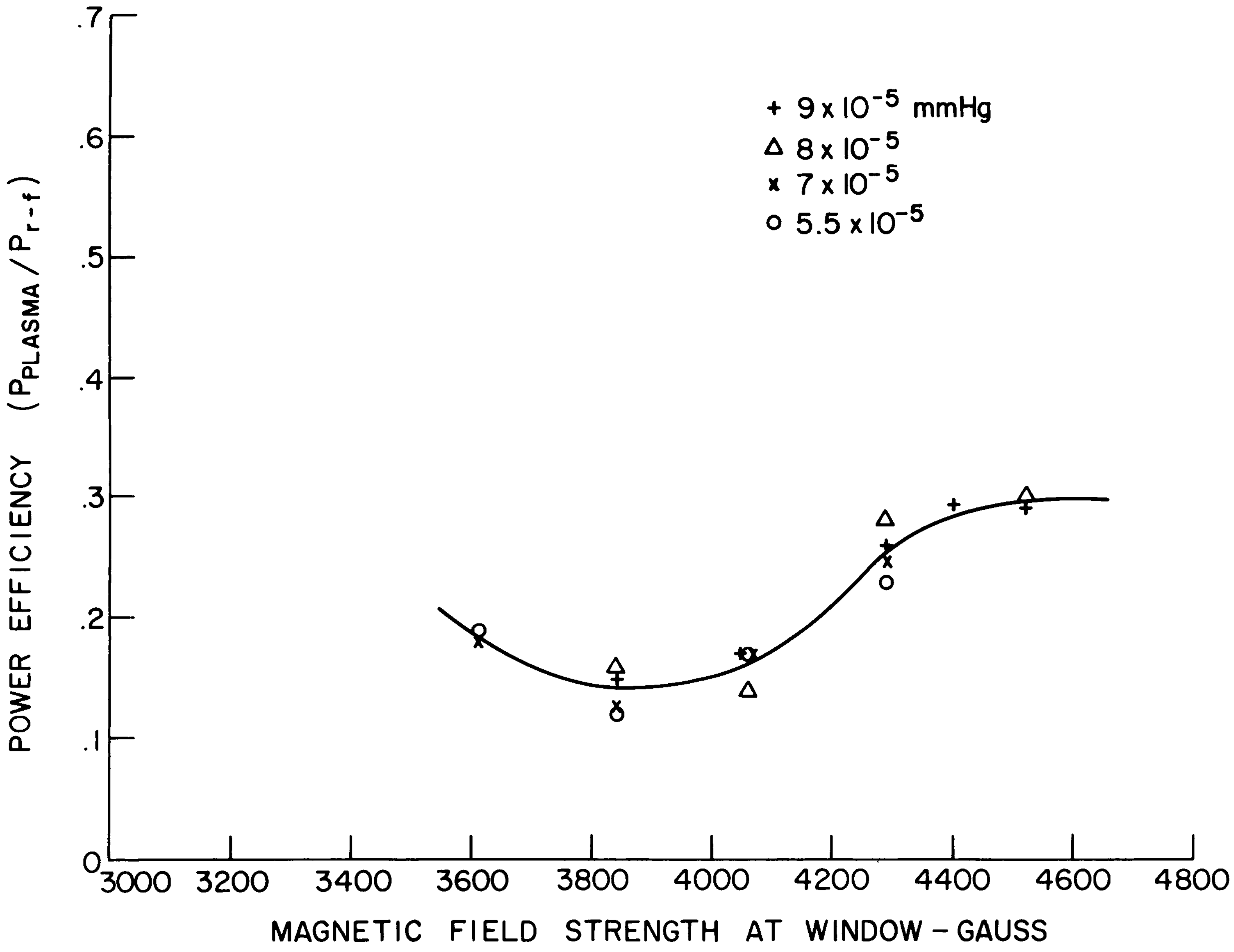

Figure 31. Dependence of Power Efficiency on Magnetic Field Strength, Krypton, 2 kw, Accelerator-to-Calorimeter Distance 43 cm, #B5 Beryllium Oxide Half-Wavelength Window, Mark IV-S Accelerator

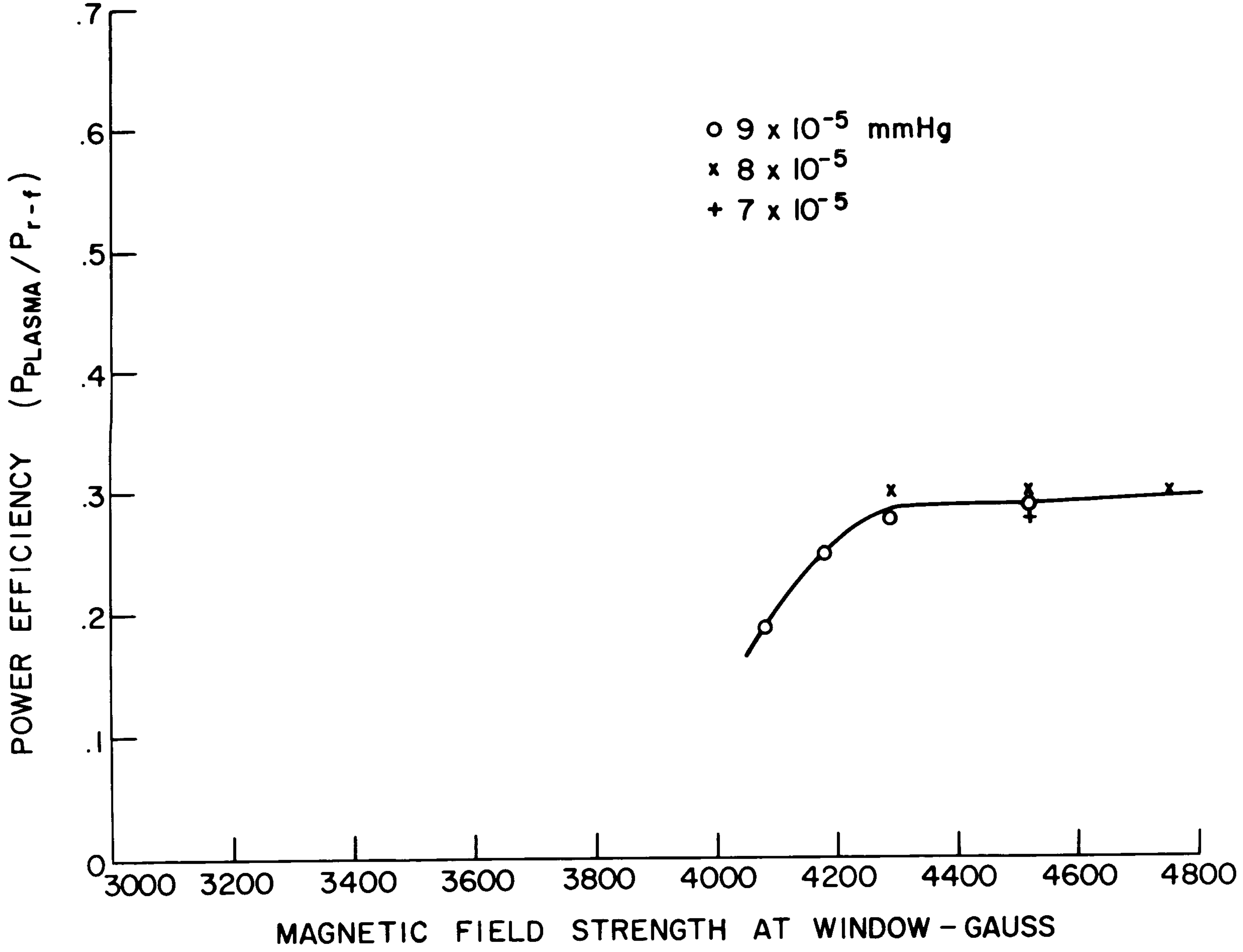

Figure 32. Dependence of Power Efficiency on Magnetic Field Strength, Xenon, 2 kw, Accelerator-to-Calorimeter Distance 43 cm. #B5 Beryllium Oxide Half-Wavelength Window, Mark IV-S Accelerator

This accelerator was more troubled by window failure than was the Mark IV-L device. This could have been due to slight dimensional differences in the shorter accelerator, although no specific cause could be discovered. As a result, however, significant tests were carried out with two windows, #B4 (Figure 28) and #B5 (Figures 29 - 32), differing only slightly in the size of the axial injection hole. The B4 window tests resulted in generally higher efficiency, attaining on one test 42%, as shown in Figure 28. The series of tests using the B5 window and varying the propellant species (Figures 29 - 32) show that optimum efficiency is essentially independent of molecular weight but that the optimum field strength increases with increasing molecular weight. Since no startling increase in efficiency resulted from shortening of the accelerator, and since in addition wall erosion continued to occur (although the wall in this case was stainless steel), it was decided to turn to the peripheral injection (Mark V) accelerators. Before making this change, however, the sampling probe array was tested briefly with the Mark IV-S accelerator in order that direct comparison with the total calorimeter could be made.

Figure 33 illustrates a three-dimensional plot of the power density distribution as obtained by the diode probes for one set of accelerator operating conditions. An average power density profile taken from the Figure 33 data is shown in Figure 34, and an average ion flux density profile for these same conditions is included as Figure 35. Numerical integrations of these curves are performed in Tables I and II. The power (64 watts) comes out to be approximately 10% of the power for these same conditions obtained with the total calorimeter (Figure 29). The ion flux (156 ma $\equiv 9.7 \times 10^{18}$ singly charged ions/sec) is approximately 10% of the injected neutral flux (.42 mg/sec $\equiv$ 9.0×10^{19} nitrogen molecules/sec).

The following causes for the lowness of the power (relative to total calorimeter measurements) can be conceived:

1. The pattern as seen from Figure 33 is somewhat irregular, with high density plasma beams being present. It is possible that some of these beams, carrying large amounts of the total plasma power,

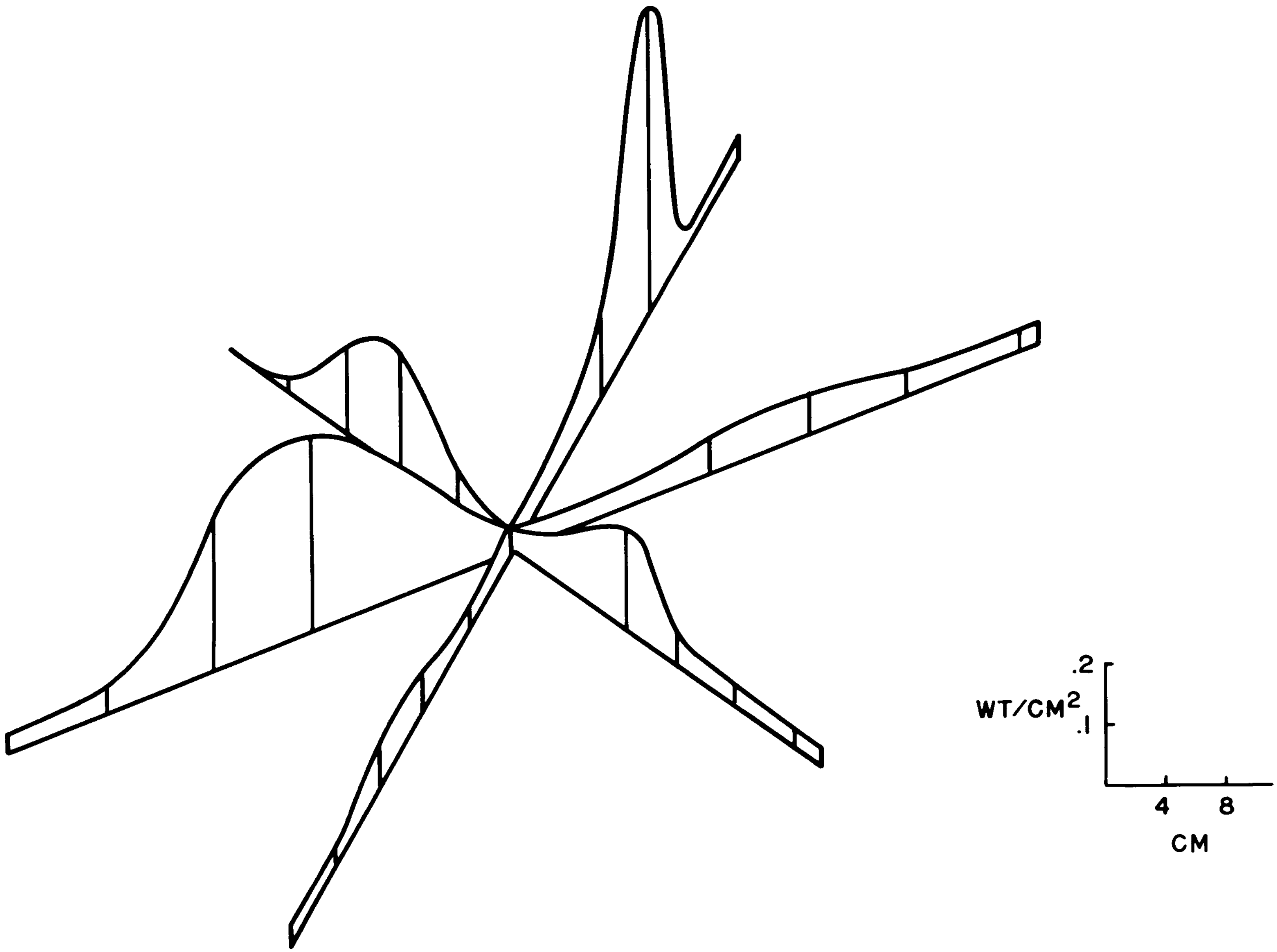

Figure 33. Power Density Contour Mark IV-S Accelerator Nitrogen, .42 mg/sec 2 kw, 3840 Gauss Accelerator-to-Array Distance: 70 cm Ambient Pressure ~ 4 x 10^{-5} Torr

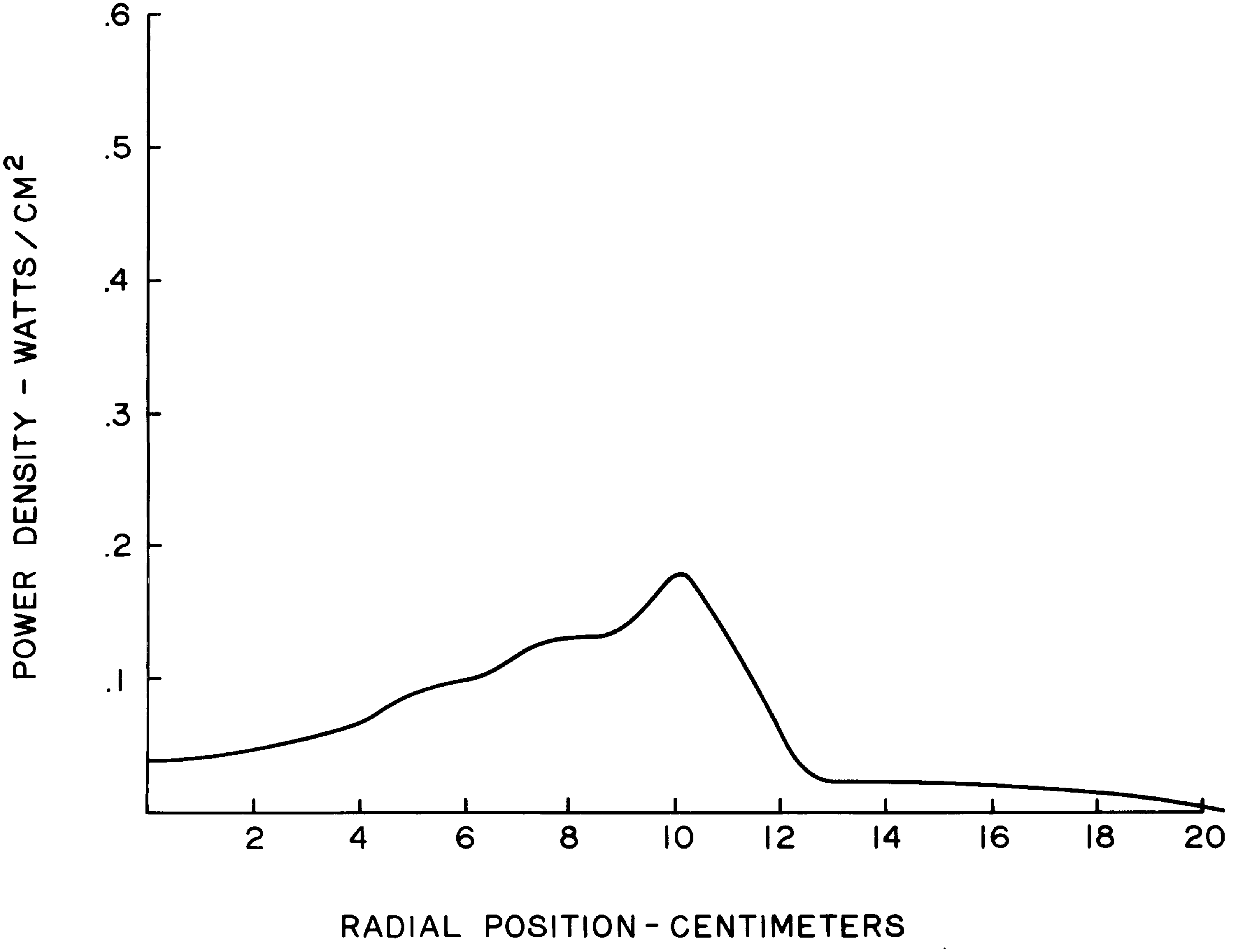

Figure 34. Power Density Profile; Mark IV-S Accelerator; Nitrogen, .42 mg/sec 2kw, 3840 Gauss Accelerator-to-Array Distance 70 cu Ambient Pressure $\sim 4\times10^{-5}$ Torr

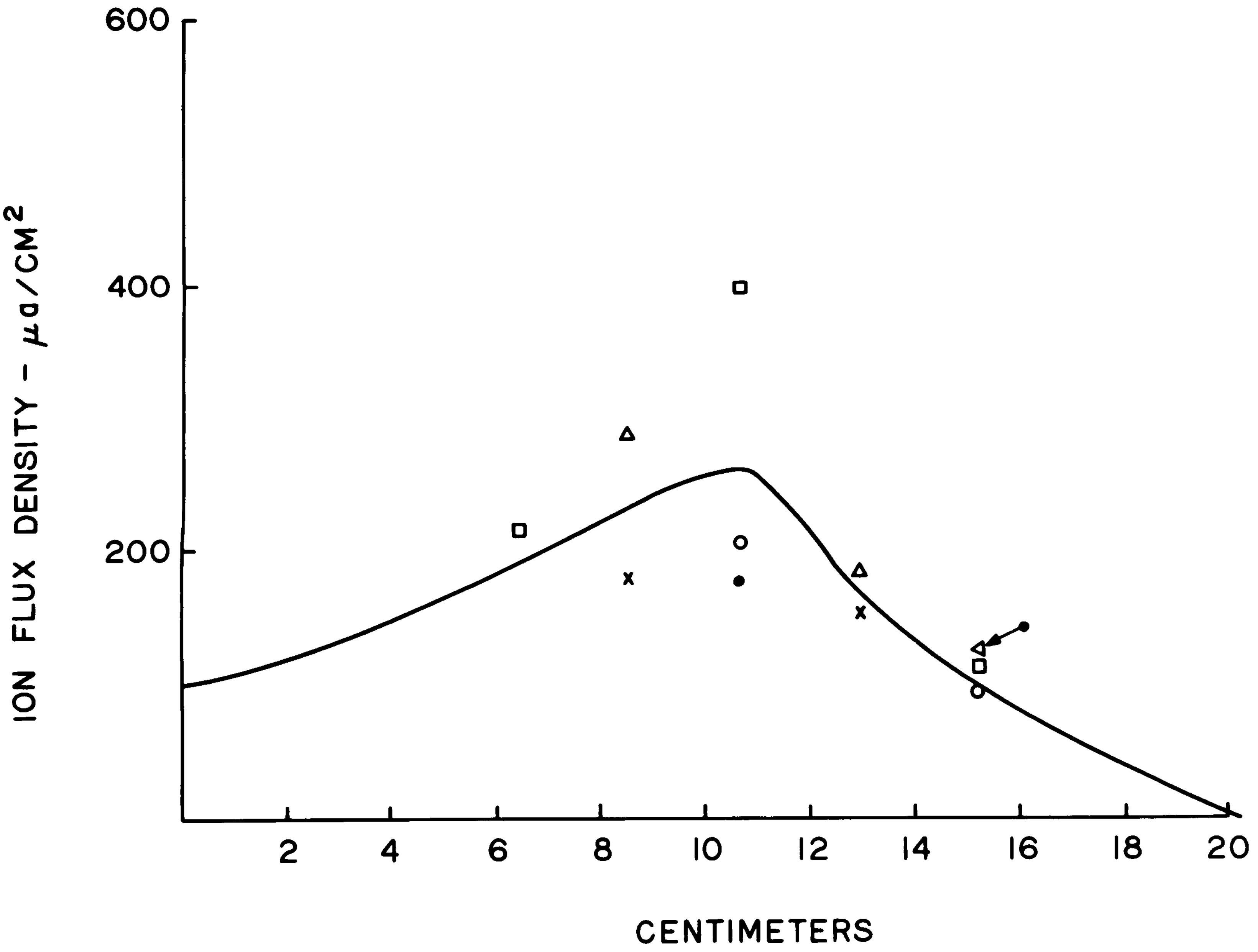

Figure 35. Ion Flux Density Profile Mark IV-S Accelerator Nitrogen, .42 mg/sec 2kw, 3840 Gauss, Accelerator-to-Array Distance 70 cu, Ambient Pressure ~4 x 10^{-3} Torr

TABLE I.

Integration of Figure 34. Exhaust Stream Power, Mark IV-S Accelerator, nitrogen, .42 mg/sec., 2 kw, 3840 gauss, accelerator-to-array distance 70 cm

r_n	$A_{n-(n-1)}$	$\bar{p}$	P
cm	cm^2	wt/cm^2	watts
1	3	.04	--
2	10	.04	--
3	15	.05	1
4	22	.06	1
5	28	.08	2
6	35	.10	4
7	41	.11	4
8	48	.12	6
9	53	.13	7
10	59	.16	9
11	66	.17	11
12	73	.08	6
13	79	.03	2
14	84	.02	2
15	90	.02	2
16	98	.02	2
17	105	.02	2
18	109	.02	2
19	117	.01	1
20	123	--	
		Total	64 watts

TABLE II.

Integration of Figure 35. Exhaust Stream Ion Flux, Mark IV-S Accelerator, nitrogen, .42 mg/sec., 2 kw, 3840 gauss, accelerator-to-array distance 70 cm.

r_n cm	$A_{n-(n-1)}$ cm^2	$\bar{i}$ $\mu a/cm^2$	I ma
1	3	110	.3
2	10	120	1.2
3	15	130	2.0
4	22	140	3.1
5	28	150	4.2
6	35	170	6.0
7	41	190	7.8
8	48	210	10.1
9	53	230	12.2
10	59	250	14.8
11	66	250	16.5
12	73	230	16.8
13	79	180	14.2
14	84	140	11.8
15	90	120	10.8
16	98	90	8.8
17	105	60	6.3
18	109	40	4.4
19	117	30	3.5
20	123	10	1.2
		Total	156.0 ma

could have been missed by the array.

2. The fact that the array was considerably further away from the engine (70 cm) than was the calorimeter (43 cm) could result in some decrease in the power, as was demonstrated in Figure 23.
3. The screens across the probe orifices would take out a certain percentage of the impinging stream. Sheaths around these screen wires could increase the effective screen "shadow" area.
4. Engine operating characteristics could have changed between the times that the total calorimeter and diode array were employed.
5. Numerical errors could exist.

Potential Probe Measurements

The potential probes were first used with the Mark IV-S accelerator. Since for these measurements the data were read from meters, only two sketchy sets of emitting and non-emitting curves were obtained during the limited times available. The forms of these curves are similar to those obtained from the Mark V-L accelerator (discussed later) and shown in Figure 36.

Although the breaks in the I-V (i.e., probe current vs. potential) curves were not as sharp as desired and did not necessarily agree with the probe voltage at which the emitting and non-emitting curves started to become mutually parallel, the plasma potentials appeared to be about +15 volts at the probes, and the probe currents were as great as 0.5 ma at +30 volts probe bias. Specifically, probe A indicated a local plasma potential of perhaps +14 volts during one accelerator run, while probe B (6.5 cm closer to accelerator than A) indicated a local plasma potential of perhaps +17 volts during the next accelerator run. Both of these values could be as high as +20 volts.

Energy Analyser Probe Measurements

In these first measurements with the energy analyser probe, the probe data were obtained point-by-point from meters. Consequently, the few points that could be read during a run gave plots which showed only the gross features of the accelerator ion energy. The curves thus obtained followed the same

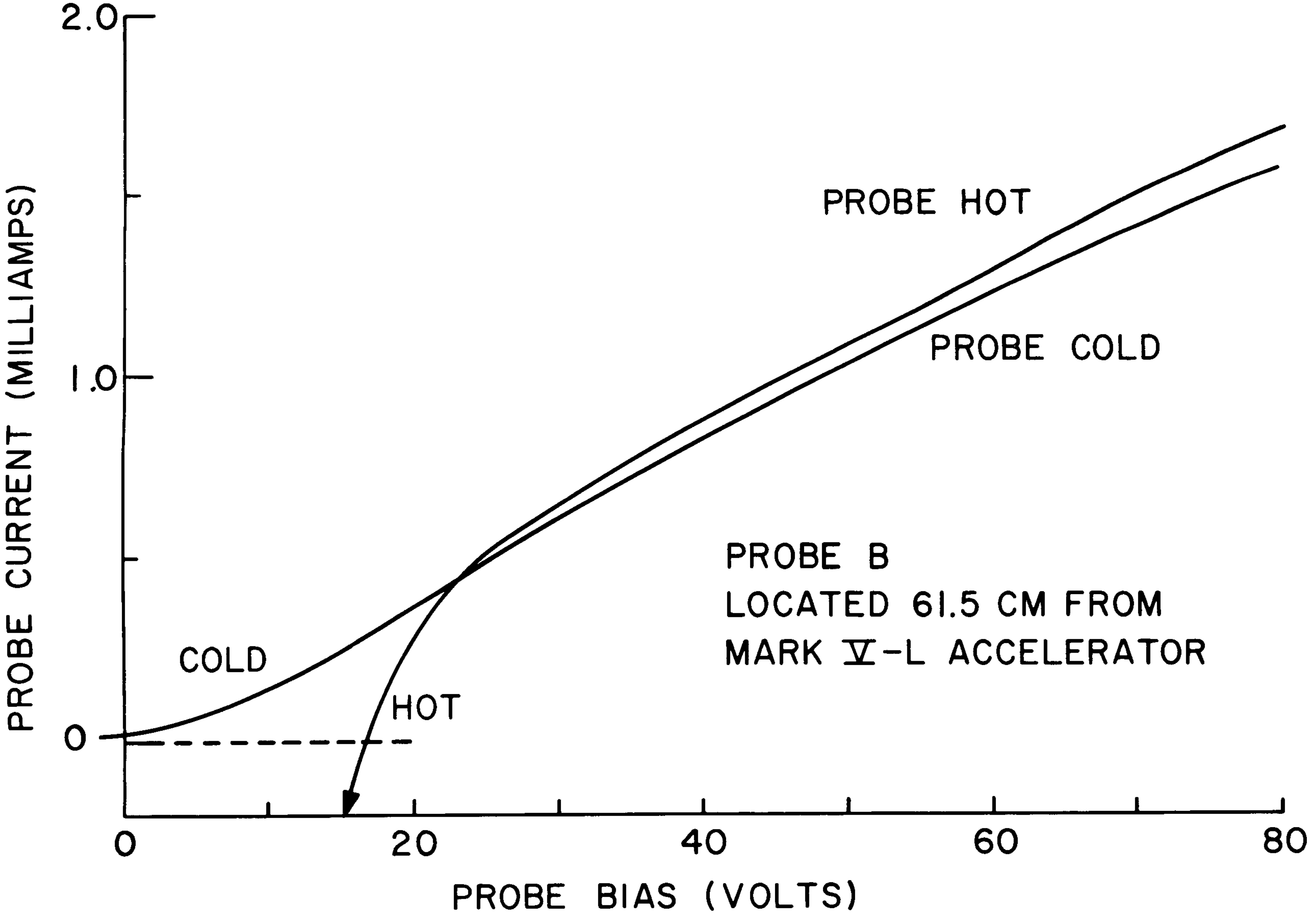

Figure 36. Typical Potential Probe Current Response with Accelerator Operating

general pattern as shown in Figure 37. Figure 37 shows an energy analyser probe I-V response curve which was obtained with an X-Y plotter in conjunction with the Mark V-L accelerator discussed elsewhere. The ion energy distribution is determined from these I-V curves by taking their derivative and plotting dI/dV vs. $(V-V_p)$ where I is probe current, V is volts, and V_p is plasma potential. For this accelerator, the potential probe indicated a plasma potential of perhaps 15 volts.

The energy analyzer probe results are indicated in Table III below.

TABLE III.

Energy Analyser Probe Measurements of the Mark IV-S Accelerator.
nitrogen, 0.42 mg/sec., 3840 gauss (at window)

Accel. rf power (kw)	Plasma Jet Ions	
	Avg. Energy (ev)	Energy Spread (ev)
2	96	28
2	~ 110	~ 50
1	85	35
3	197	71

Before obtaining the I-V curves which led to these results, it was determined that for a Mark IV-S two-kilowatt accelerator run, at least -70 volts was required on the electron repelling grid to eliminate all electron current at the positive plate. Consequently, repelling grid potentials of -100 volts or -150 volts (for 3 kw run) were used in all cases.

It can be concluded first that the energy analyser probe operated as expected. Since no ion current exceeded 30 microamperes total (< 0.1 milliamp cm^{-2}), no space charge limiting could have occurred. As discussed elsewhere, the space charge limit for this probe was calculated to be about 2 milliamps cm^{-2}.

As to the probe results, we see from Table III that the main body of ions tend to reach the energy analyser probe with energy spreads of 30-70 electron volts and average $e(V-V_p)$ energies of about 85-200 electron volts,

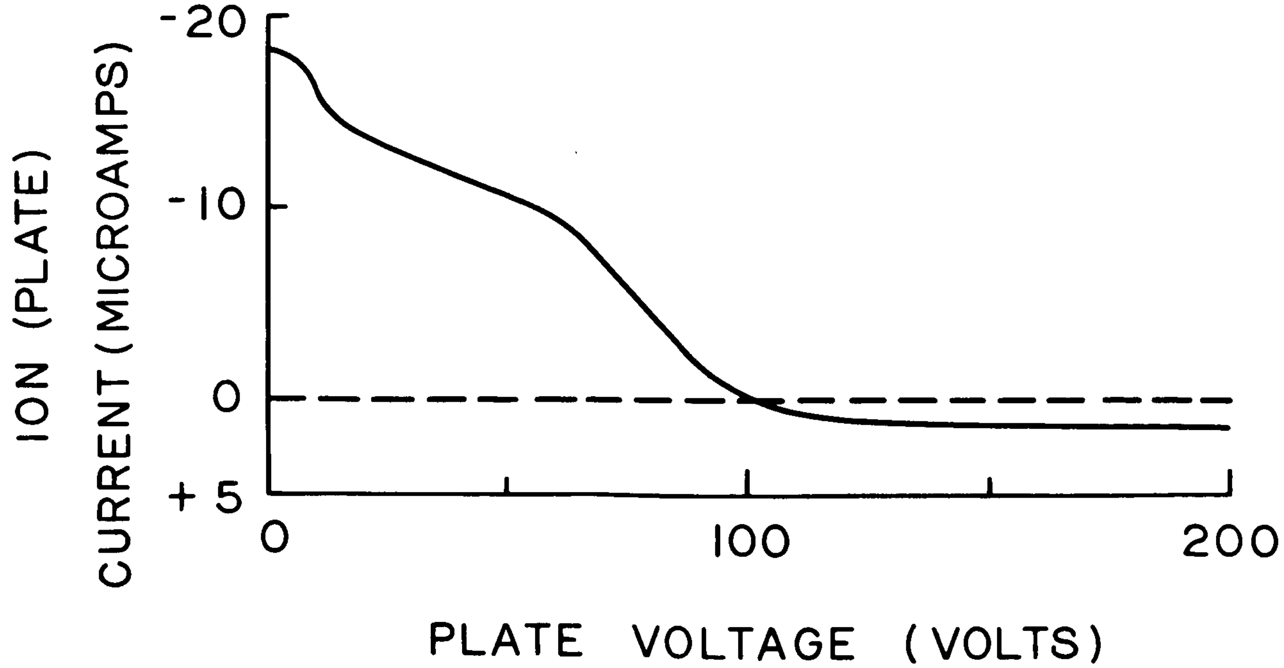

Figure 37. Energy Analyser Probe Response Curve. Probe is Located 68 cm fromMark V-L Accelerator, with Probe Electron Repelling Grid Biased at -250 Volts

the average energy increasing as the rf power level is increased from one to three kilowatts. This trend is as expected. However, an interesting result is that the lowest rf power level runs of the accelerator appeared to yield the highest ion currents.

3.3 Mark V-L Accelerator (Peripheral-injection, long version)

Since there is considerable effort involved in setting up and removing the probe array, initial tests on the Mark V-L accelerator were made using the array since it was already in position from the final Mark IV-S tests. Power density and ion flux density curves for one operating point are shown in Figures 38, 39 and 40. The power and ion flux integrations are performed in Tables IV and V. The total stream power is approximately 3 times the power calculated in Table I for the Mark IV-S accelerator; if an equivalent ratio of probe-obtained to calorimeter-obtained power exists for the Mark V-L as for the Mark IV-S accelerator, one can expect very favorable efficiency for the peripheral injection device; this must, of course, be verified by actual total calorimeter tests. The ion flux (41.2 ma $\equiv 2.6 \times 10^{17}$ singly-charged-ions/sec) is again quite a bit less than the injected neutral flux (.28 mg/sec 4.2×10^{18} argon molecules/sec).

If 20 cm is taken as the outer radius of the stream at 70 cm, as seems reasonable from Figures 38, 39 and 40, then a 16° half angle results for the plasma stream. Since the outer limit of the stream has not actually been reached in these measurements, however, it would be well to remeasure the stream with the array located closer to the accelerator.

Potential Probe Measurements

The potential probes were used on several runs of the Mark V-L accelerator. Since for these runs the current and voltage data were recorded on an X-Y plotter, the curves are better and much more numerous than was the case with the Mark IV-S accelerator already discussed.

To determine the potential probe emission current (I) as a function of potential difference (V) between probe and surroundings, the probe I-V

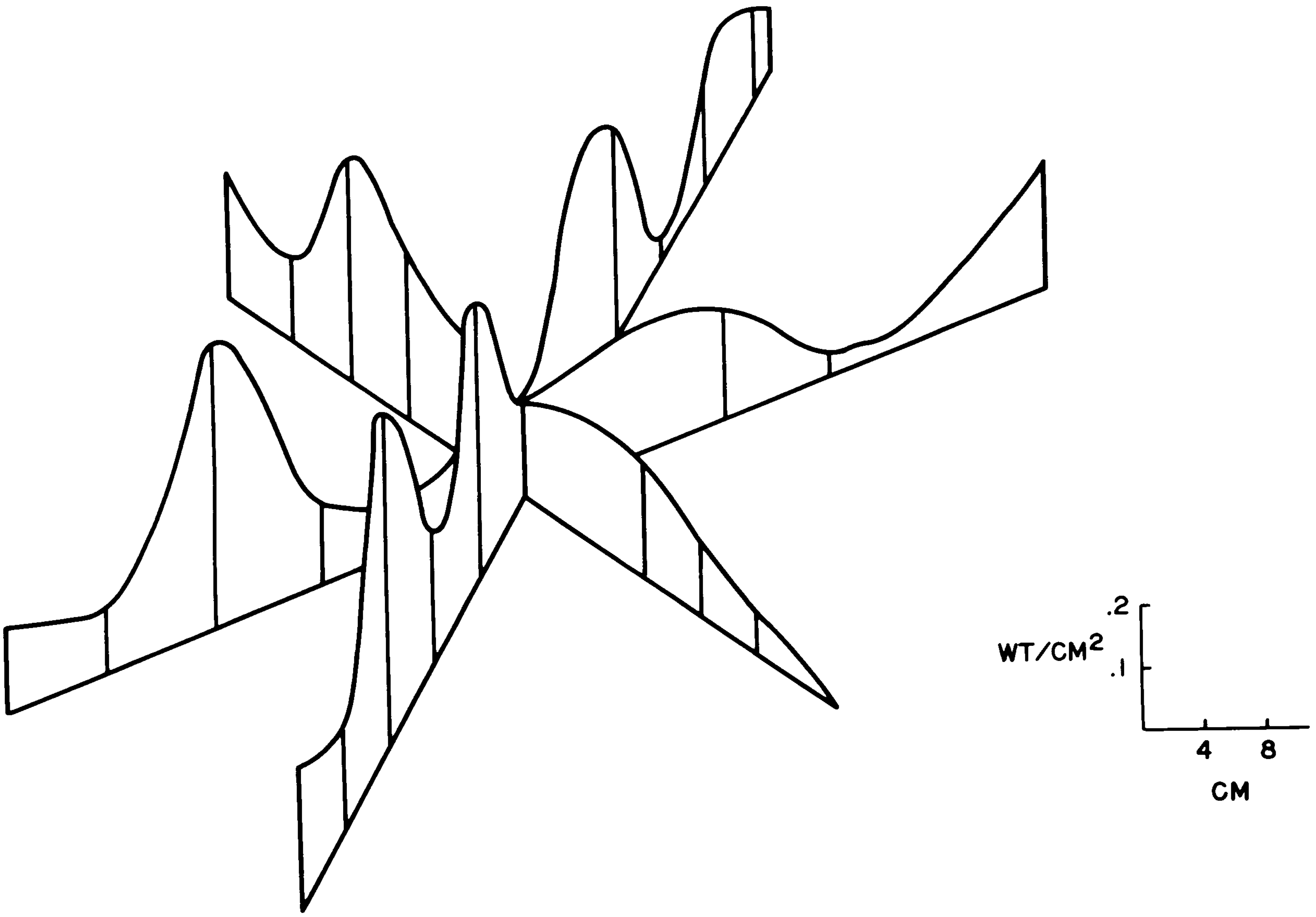

Figure 38. Power Density Contour Mark V-L Accelerator Argon, .28 mg/sec 2kw, 3730 Gauss Accelerator-to-Array Distance 70 cu, Ambient Pressure 2.5 x 10^{-5} Torr

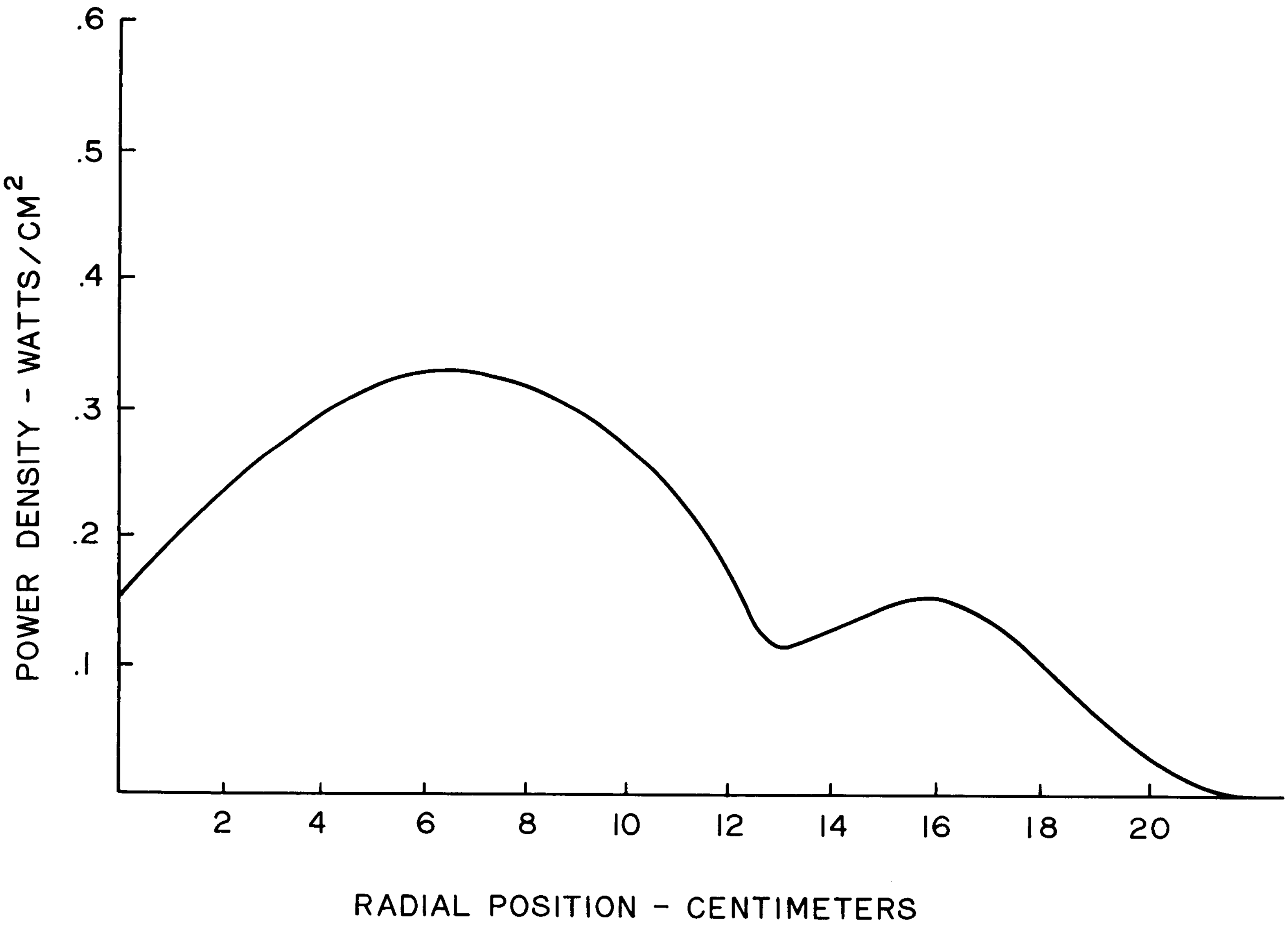

Figure 39. Power Density Profile Mark V-L Accelerator Argon, .28 mg/sec 2kw, 3730 Gauss Accelerator-to-Array Distance 70 cm Ambient Pressure 2.5 x 10^{-5} Torr

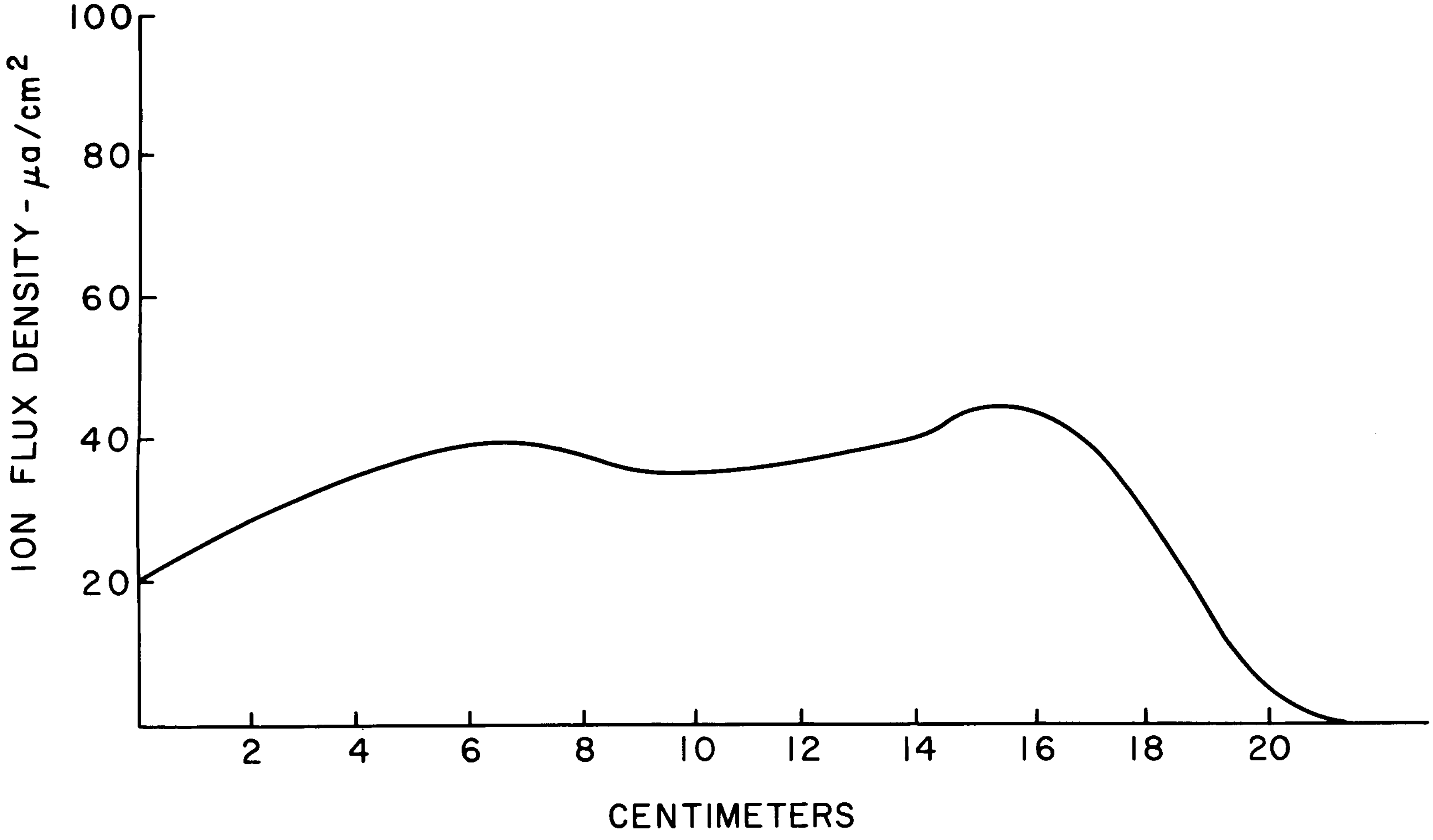

Figure 40. Ion Flux Density Profile Mark V-L Accelerator Argon, .28 mg/sec 2 kw, 3730 Gauss Accelerator-to Array Distance 70 cm Ambient Pressure 2.5 x 10^{-5} Torr

TABLE IV.

Integration of Figure 39. Exhaust Stream Power, Mark V-L Accelerator, argon, .28 mg/sec., 2 kw, 3730 gauss, accelerator-to-array distance 70 cm

r_n	$A_{n-(n-1)}$	$\bar{p}$	P
cm	cm^2	wt/cm^2	wt
1	3	.20	1
2	10	.23	2
3	15	.27	4
4	22	.29	6
5	28	.31	9
6	35	.33	12
7	41	.32	13
8	48	.31	15
9	53	.30	16
10	59	.27	16
11	66	.23	15
12	73	.17	12
13	79	.11	9
14	84	.12	10
15	90	.14	13
16	98	.15	15
17	105	.13	14
18	109	.08	9
19	117	.05	6
20	123	.02	2
		Total	199 watts

TABLE V.

Integration of Figure 40. Exhaust Stream Ion Flux, Mark V-L Accelerator, argon, .28 mg/sec., 2 kw, 3730 gauss, accelerator-to-array distance 70 cm.

r_n	$A_{n-(n-1)}$	$\bar{i}$	I
cm	cm^2	$\mu a/cm^2$	ma
1	3	24	.1
2	10	28	.3
3	15	32	.5
4	22	34	.7
5	28	37	1.1
6	35	39	1.4
7	41	39	1.6
8	48	37	1.8
9	53	35	1.9
10	59	35	2.1
11	66	36	2.4
12	73	37	2.7
13	79	38	3.0
14	84	40	3.4
15	90	43	3.9
16	98	43	4.2
17	105	40	4.2
18	109	29	3.2
19	117	18	2.1
20	123	5	.6
		Total	41.2 ma

curves were measured when emitting in the accelerator testing tank, but with the accelerator not operating. These curves are shown in Figure 41 for both probes A and B. Since the emission current of both probes was -0.03 milliamps at V = 0 volts, this value was used at the "break" in the emitting probe plasma I-V curves so as to aid in estimating the plasma potential at the probe position. Of course, in a plasma the probe-"collector" distance (sheath thickness) is smaller than in the case of no plasma where the plasma sheath thickness is replaced by the probe-to-tank wall and probe support distance. Consequently, in a plasma the probe emission currents can be much greater than shown in Figure 41.

A typical plasma potential curve during accelerator operation is shown in Figure 36. In this series of measurements, saturated probe currents at +50 volts bias varied from 0.4 to about 7 milliamps. As shown in Figure 36, the emitting probe current normally did not coincide with the non-emitting current at bias voltage > V_p (local plasma potential), nor were the two curves always straight or parallel at bias voltage > V_p. Since the plasma potential was not always clearly indicated by the I-V curves, V_p was estimated (in order of credibility) first from the "break" in the emitting curve and second from the divergence from parallel of the emitting and non-emitting curves. Any "knee" in the non-emitting I-V curve was usually too ill-defined to be useful. As indicated earlier, probe A was 2 cm ahead of the diode probes and 68 cm from the accelerator exit, while probe B was 8.5 cm ahead of the diode probes and 61.5 cm from the accelerator exit. Part way through the runs, probe A developed a short to ground, after which only probe B data was obtained.

All but three of the 22 plasma potentials were between +16 and +25 volts from ground. In those few cases where both probes A and B were operated during the same run, probe B showed a 5-7 volt higher V_p than probe A.

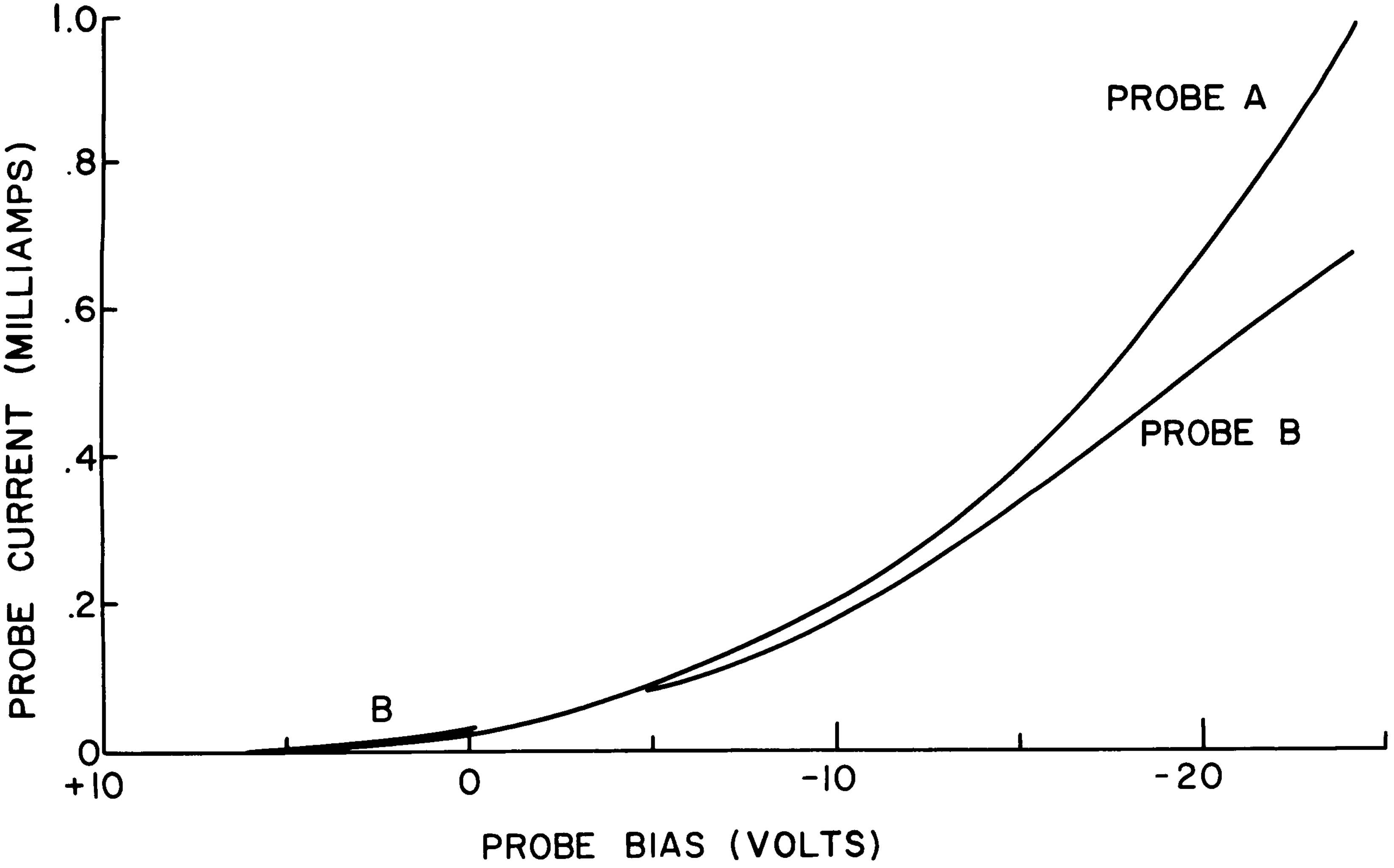

Figure 41. Hot Potential Probe Emission Current in Vacuum Tank. No Plasma Present

Energy Analyser Probe Measurements

For the Mark V-L accelerator measurements, the energy analyser probe data were recorded with an X-Y plotter. This yielded probe response I-V (current-voltage) curves such as shown in Figure 37. As mentioned elsewhere, the ion energy distribution is determined from these I-V curves by plotting dI/dV vs. $(V-V_p)$, where I is (ion) current, V is probe plate voltage, and V_p is local plasma potential. For this accelerator, the potential probe usually indicated plasma potentials of about 20 volts in the vicinity of the energy analyser probe.

The energy analyser probe results are indicated in Table VI.

TABLE VI.

Energy Analyser Probe Measurements of the Mark V-L Accelerator.

Accel. Conditions			Plasma Jet Ions	
rf Power (kw)	Gas	Gas Flow (mg/sec)	Avg. **Energy** (ev)	Energy Spread (ev)
1	N_2	0.42	62	31
1.5	Ar	0.22	61	38
2	Ar	0.26	57	41

Only three analyser probe runs were made on the Mark V-L accelerator because grid to plate leakage developed during the third analyser probe run, and rapidly became too serious for further use of the probe. However, for these three runs, we see that the main body of ions appears to reach the energy analyser probe with an energy spread of 30-40 electron volts, and in all cases with an average $e(V-V_p)$ energy of about 60 electron volts.

Another feature of these energy analyser probe I-V curves (see Figure 37) is the indication of another, smaller, body of particles centering at about -8 electron volts $[\, e(V-V_p)]$. In Figure 37 this group is indicated at a slightly positive potential because V_p has not yet been subtracted from the potential. This group of particles might be due to a relatively quiescent ion gas which enters the probe with little or no directed energy. Such a quiescent ion gas might be produced through collision of accelerator ions or electrons with any vacuum chamber ambient gas. That these particles center at an $e(V-V_p)$ energy of -8 rather than zero electron volts, is not understood, unless the V_p used is in error by that amount. This low energy group of particles may also have been present in the Mark IV-S runs reported elsewhere, but their presence would not have been discovered due to the very few data points read in that voltage range (X-Y plotter not used there).

4. SUMMARY AND CONCLUSIONS

Two basically new things have been done during these six months. Axial-injection accelerators having a one-inch bore have been operated continuously for several minutes at a time in the 2 kilowatt range, and a sampling probe array which can simultaneously map the exhaust stream power density ion flux density and ion velocity distribution has been successfully employed. In each case, however, serious disadvantages have been revealed which detract from the applicability of either accomplishment. The axial injection accelerator has been shown to have inferior power efficiency and basic structural weaknesses. The probe array (and in particular the diode probe) is suspected to be yielding a substantially lower than actual power value; it is reasonable to assume that the resulting ion flux value is also too small, an assumption strengthened by the lowness of the measured ion flux relative to injected neutral flux.

The light bulb filament-type emitting probe appears to be useful in estimating the local plasma potential (V_p). However, the frequent failure of the I-V curves to become straight and the frequent failure of the emitting and non-emitting I-V curves to coincide at bias voltages above V_p render the method less decisive for determining plasma potential than could be desired. The non-ideal coiled shape of these filaments is probably the primary cause of this problem. In addition we have the problem that even with the probe biased at V_p there is some tendency for a hot probe to emit electrons. This makes less certain the relationship between the emitting I-V curve "break" and V_p. Thus, the I-V curve "knee" of a straight or flat non-emitting probe might yield a better or more certain value for V_p.

The energy analyser probe appears to have worked well, except that after exposure to perhaps 15-30 minutes of accelerator operation the probe developed grid-plate and grid-ground leakage (see Figure 18). Upon later disassembling the probe the inside (edge) surfaces of the Teflon insulators were found to be coated with metal. This metal was not necessarily from sputtering off the grids since the outside of the probe body and other objects also (normally) were coated to at least some extent. The probe design will have to be altered to reduce its susceptibility to metal deposits.

This six-month period ended in the optimistic result that the peripheral injection accelerator is possibly a good deal more efficient than is the axial injection device. This must be verified, however, by total calorimeter measurements.

5. PROGRAM PLANS

The next immediate task is to evaluate the Mark V (peripheral injection) accelerators using the total calorimeter. Completion of the thrust stand is expected soon so that hopefully an independent, absolute measurement of thrust and therefore of mass utilization will be available. The inability of the diode array to measure power accurately will be considered. Improvements in the potential probes and in the energy analyser probe will be explored.

REFERENCES

1. D. B. Miller, "Continuous Microwave Magnetic Accelerator," Final Report - Contract No. NAS3-3567, pp. 67, 80-85, August 1964.
2. C. G. Suits, "The Collected Works of Irving Langmuir," Volume IV, page 372, Pergamon Press, N. Y., N. Y. (1961).
3. K. T. Yen, "Microwave Reflection by Non-Uniform Plasmas with Exponential Electron Distribution," J. App. Phys. 35, 290, 1964.
4. C. R. Mullin, E. D. Shane, "Comment on Microwave Reflection by Non-Uniform Plasmas with Exponential Electron Distribution," Proc. IEEE 52, 1272, 1964.

DISTRIBUTION LIST FOR SEMIANNUAL REPORT
CONTRACT NAS3-6266

NASA Headquarters (2)
FOB-10B
600 Independence Avenue, N. E.
Washington, D.C.
Attn: RNT/J. Lazar

NASA-Marshall Space Flight Center (1)
Huntsville, Alabama
Attn: E. Stuhlinger

Commander (1)
Aeronautical Systems Division
Wright-Patterson AFB, Ohio
Attn: ASRMPE/R. River

NASA-Lewis Research Center (1)
Electromagnetic Propulsion Division
21000 Brookpark Road
Cleveland, Ohio 44135
Attn: G. Seikel

NASA-Lewis Research Center (1)
Electromagnetic Propulsion Division
21000 Brookpark Road
Cleveland, Ohio 44135
Attn: W. Moeckel

NASA-Lewis Research Center (2)
Spacecraft Technology Division
21000 Brookpark Road
Cleveland, Ohio 44135
Attn: J. H. Childs

NASA Headquarters (1)
FOB-10B
600 Independence Avenue, N.E.
Washington, D.C.
Attn: RNT/J. Mullin

General Dynamics/Astronautics (1)
P.O.Box 1128
San Diego, California 92112
Attn: Dr. T. Gooding

General Electric Company (1)
Valley Forge Space Technology Center
P. O. Box 8555
Philadelphia 1, Pennsylvania
Attn: Dr. P. Gloersen

Electro-Optical Systems, Inc. (1)
125 North Vinedo Avenue
Pasadena, California
Attn: Dr. Gordon Cann

AVCO-Everett Research Laboratory (1)
A Division of AVCO Corporation
2385 Revere Beach Parkway
Everett 49, Massachusetts
Attn: Dr. S. Janes

Allison Division (1)
General Motors Corporation
Indianapolis, Indiana
Attn: Mr. T. Rosebrock

Litton Industries (1)
Beverly Hills, California
Attn: Dr. A. Penfold

Research Division (1)
American Radiator and Standard Corp.
P.O.Box 2003
New Brunswick, New Jersey
Attn: Mr. E. C. Okress

TRW Space Technology Laboratories (1)
Thompson Ramo Wooldridge Inc.
One Space Park
Redondo Beach, California
Attn: Mr. C. L. Dailey

Massachusetts Institute of Technology (1)
Cambridge 39, Massachusetts
Attn: Dr. E. Covert

AFWL (1)
WLPC/Capt. C. F. Ellis
Kirtland Air Force, New Mexico

NASA-Lewis Research Center (2)
21000 Brookpark Road
Cleveland, Ohio 44135
Attn: Library

NASA-Lewis Research Center (1)
21000 Brookpark Road
Cleveland, Ohio 44135
Attn: Report Control Office

NASA-Lewis Research Center (1)
Spacecraft Technology Procurement Section
21000 Brookpark Road
Cleveland, Ohio 44135
Attn: Mr. John H. DeFord

NASA Scientific and Technical Information Facility (6)
Box 5700
Bethesda 14, Maryland
Attn: NASA Representative RQT-2448

NASA-Lewis Research Center (15)
Spacecraft Technology Division
21000 Brookpark Road
Cleveland, Ohio 44135
Attn: Dr. H. G. Kosmahl

NASA-Lewis Research Center (1)
21000 Brookpark Road
Cleveland, Ohio 44135
Attn: Technology Utilization Office

Aerospace Corporation (1)
P. O. Box 95085
Los Angeles, California 90045
Attn: Library Technical Documents Group

Westinghouse Astronuclear Laboratories (1)
Pittsburgh 34, Pennsylvania
Attn: H. W. Szymanowski, Mgr.
Electrical Propulsion Laboratory

Radio Corporation of America (1)
Astro Electrical Division
Princeton, New Jersey
Attn: Dr. W. H. Hendel

General Technology Corporation (1)
3510 Torrance Boulevard
Torrance, California
Attn: Dr. S. Ridgeway

Republic Aviation (1)
Farmingdale, Long Island, New York 11735
Attn: Mr. A. Kunen

United States Atomic Energy Commission (1)
Division of Technical Information Extension
Oak Ridge, Tennessee